A centronuclear myopathy-dynamin 2 mutation impairs skeletal muscle structure and function in mice

Anne-Cécile Durieux, Alban Vignaud, Bernard Prudhon, Mai Thao Viou, Maud Beuvin, Stéphane Vassilopoulos, Bodvael Fraysse, Arnaud Ferry, Jeanne Lainé, Norma Beatriz Romero, et al.

A centronuclear myopathy-dynamin 2 mutation impairs skeletal muscle structure and function in mice.

Anne-Cécile Durieux[1,2,3,4], Alban Vignaud[1,2,3,4], Bernard Prudhon[1,2,3,4], Mai Thao Viou[1,2,3,4], Maud Beuvin[1,2,3,4], Stéphane Vassilopoulos[1,2,3,4], Bodvaël Fraysse[1,2,3,4], Arnaud Ferry[1,2,3,4], Jeanne Lainé[1,2,3,4], Norma B. Romero[1,2,3,4,5], Pascale Guicheney[1,6], Marc Bitoun[1,2,3,4,*].

[1] Université Pierre et Marie Curie-Paris 6, IFR14, Paris, F-75013, France.

[2] CNRS, UMR 7215, Paris, France.

[3] Inserm, U974, Paris, F-75013, France

[4] Institut de Myologie, Paris France.

[5] AP-HP, Groupe Hospitalier Pitié-Salpêtrière, Paris, F-75013, France.

[6] Inserm, U956, Paris, F-75013, France.

* Corresponding Author: Dr. Marc Bitoun,

Inserm U974, Institut de Myologie,

Groupe Hospitalier Pitié-Salpêtrière,

47, bld de l'hôpital,

75651 Paris cedex 13, France.

E-mail: m.bitoun@institut-myologie.org

Tel: 33 (0) 1.42.16.57.18

Fax: 33 (0) 1.42.16.57.00

Abstract

Autosomal dominant centronuclear myopathy (AD-CNM) is due to mutations in the gene encoding dynamin 2 (DNM2) involved in endocytosis and intracellular membrane trafficking. To understand the pathomechanisms resulting from a DNM2 mutation, we generated a knock-in mouse model expressing the most frequent AD-CNM mutation (KI-*Dnm2*^{R465W}). Heterozygous mice developed a myopathy showing a specific spatial and temporal muscle involvement. In the primarily and prominently affected *tibialis anterior* muscle, impairment of the contractile properties was evidenced at weaning and was progressively associated with atrophy and histopathological abnormalities mainly affecting mitochondria and reticular network. Expression of genes involved in ubiquitin-proteosome and autophagy pathways were up-regulated during DNM2-induced atrophy. In isolated muscle fibers from wild-type and heterozygous mice, Dnm2 localized in regions of intense membrane trafficking (I-band and perinuclear region) emphasizing the pathophysiological hypothesis in which DNM2-dependent trafficking would be altered. In addition, heterozygous fibers showed an increased calcium concentration as well as an intracellular Dnm2 and dysferlin accumulation. A similar dysferlin retention, never reported so far in congenital myopathies, was also demonstrated in biopsies from DNM2-CNM patients and can be considered as a new marker to orientate direct genetic testing. Homozygous mice died during the first hours of life. Impairment of clathrin-mediated endocytosis, demonstrated in homozygous embryonic fibroblasts, could be the cause of lethality. Overall, this first mouse model of DNM2-related myopathy shows the crucial role of DNM2 in muscle homeostasis and will be a precious tool to study DNM2 functions in muscle, pathomechanisms of DNM2-CNM and developing therapeutic strategies.

Introduction.

Centronuclear myopathies (CNM) are rare congenital myopathies including the X-linked recessive myotubular myopathy due to myotubularin mutations and the autosomal dominant and recessive CNM associated with *dynamin 2* (*DNM2*) and *BIN1/amphiphysin 2* mutations, respectively (1). Heterozygous *DNM2* mutations are associated with a wide clinical spectrum from slowly progressive CNM beginning in childhood or adolescence (2) to more severe sporadic forms with neonatal onset (3). The most frequent clinical features of DNM2-CNM are delayed motor milestones, facial and muscle weakness, ptosis, and ophthalmoplegia (4). Muscle imaging showed an initial and prominent distal involvement (4, 5). The most characteristic histological features are nuclear centralization, predominance and hypotrophy of slow-oxidative muscle fibers and radial distribution of sarcoplasmic strands (6). *DNM2* mutations were also involved in dominant intermediate and axonal Charcot-Marie-Tooth peripheral neuropathy (7, 8). If clinical overlap does exist between these two pathologies (4, 9), patients usually harbor a tissue-specific disorder affecting either skeletal muscle or peripheral nerve.

The large GTPase DNM2, ubiquitously expressed, has been involved in clathrin-dependent and clathrin-independent endocytosis, intracellular membrane trafficking and tightly interacts with the actin and microtubule networks (10-12). However, the pathomechanisms associated with the *DNM2* mutations are still largely unknown. *In vitro* studies have demonstrated that the CNM- and CMT-related DNM2 mutants impair membrane trafficking or cytoskeleton–dependent processes probably by a dominant negative effect (8, 13, 14). In addition, GFP-DNM2-mutants failed to be correctly targeted to the centrosome when transfected in fibroblast primary cells, suggesting that *DNM2* mutations might interfere with centrosome function (2). CMT-related DNM2 mutants can also disorganize the

microtubule cytoskeleton (8) and one particular CMT mutant impairs microtubule-dependent membrane transport (14). However, to date, no data is available on the impact of DNM2 mutant *in vivo*, especially in muscle fibers. In this context, we constructed a knock-in (KI) mouse model expressing the most frequent CNM-related *DNM2* mutation, i.e. an arginine-to-tryptophan substitution in position 465 located in the middle domain of the protein (p.R465W).

In this study we demonstrate that heterozygous (HTZ) *DNM2* mutation in mice induces a myopathy in which impairment of contractile properties precedes muscle atrophy and structural disorganization. Our results suggest that atrophy occurs through activation of proteasome and autophagy pathways. We also evidenced an alteration of dysferlin subcellular distribution and this was confirmed in muscle biopsies from DNM2-CNM patients. Homozygous (HMZ) KI-mice die within 24 hours after birth. We evidenced a defect in endocytosis which could be the cause of neonatal lethality. Finally, we demonstrate that Dnm2 localized in areas of rich membrane trafficking activity both in WT and HTZ muscle fibers. This reinforces the idea of a dominant negative effect of the mutation on DNM2-dependent trafficking.

Results.

Generation of transgenic mice and behavioural study. KI-*Dnm2*^{R465W} mice were created in C57BL/6 genetic background by homologous recombination using standard techniques (Materials and Methods and Fig. 1 A-C). Quantitative RT-PCR and western blot analyses in homogenates extracted from hindlimb skeletal muscles from heterozygous KI-*Dnm2*$^{R465W/+}$ (HTZ) and homozygous KI-*Dnm2*$^{R465W/R465W}$ (HMZ) neonates showed that Dnm2 expression was not altered by the mutation when compared to wild-type (WT) animals (Fig. 1 D-E). Dnm2 protein was expressed in all tested tissues including liver, lung, heart, and diaphragm (data not shown). Analysis of 297 newborn mice resulting from HTZ intercrosses showed that WT, HTZ and HMZ were born at a ratio of 100:169:28. The non-mendelian ratio reflects the HMZ neonatal lethality leading to underestimation of their number. Indeed, 98% of HMZ died during the first 24 hours of life and only 6 homozygous mice survived until weaning. One of them was sacrified before death at 22-day-old for histological analysis (see below). At birth, all pups developed normally but HMZ were 15% lighter than WT and HTZ littermates (HMZ weight versus (vs) WT and HTZ littermate values, $P < 0.001$). The HTZ male and female adult mice, lived as long as WT and no change in body weight nor growth curves were observed (Fig. 2 A). Relative to body weight, the mass of most of the organs was unchanged in HTZ mice when compared to age-matched WT (Fig. S1). In this study, we therefore focused on male mice. Locomotor activity, assessed by openfield and endurance performance tested at 2 and 8 monthsof age, were unchanged in HTZ (Fig. 2 B).

Heterozygous mice develop muscle atrophy. Muscle atrophy started at 2 months and worsened at 8 months. *Tibialis anterior* (TA) was the first affected muscle at 2 months (Fig. 2 C). At this age, *soleus* and diaphragm muscles of HTZ mice showed a transient increase of

mass whereas quadriceps, *gastrocnemius/plantaris* group and *extensor digitorum longus* (EDL) muscles were spared (Fig. 2 C and Fig. S1). At 8 months of age, TA muscle remained lower than WT and atrophy became significant in *gastrocnemius/plantaris* group and quadriceps muscles. We studied the expression of some of the genes overexpressed during various atrophy processes. At 2 months of age, FOXO3a transcript was up-regulated and this was associated with an increase of the active dephosphorylated form translocation into the nucleus (Fig. 3). Both ubiquitin-proteasome and autophagy pathways were activated by this common transcription factor as evidenced by the significant increase of MuRF1 and Gabarapl1. At 8 months, all values returned to basal level except for Atrogin1 which was significantly down-regulated (Fig. 3). Expression of FOXO3a, MurF1, Atrogin1 and Gaparapl1 was evaluated in muscle biopsies from 2 DNM2-CNM patients (42 and 50-year-old) and 2 age-matched healthy control subjects using hypoxanthine guanine phosphoribosyl transferase (HPRT) gene as control (Fig. S2). FOXO3a and Gabarapl1 were overexpressed only in one patient.

Histomorphology and ultrastructure analyses. TA muscle was stained with standard histological and histochemical techniques. From 3 weeks to 8 months of age, hematoxylin and eosin (HE) staining showed normal angular fibers. There was no sign of inflammation, regeneration nor connective tissue accumulation between muscle bundles and fibers (Fig. 4 A, D, G). The percentage of internalized and/or centralized nuclei did not exceed 2% in both WT and HTZ mice. The most striking feature of HTZ muscles was observed on reduced nicotinamide adenine dinucleotide-tetrazolium reductase (NADH-TR) staining revealing intermyofibrillar disorganization. Indeed, mitochondria and sarcoplasmic reticulum showed an abnormal central accumulation in 10% of fibers at 2 months and this reached 30% at 8 months (Fig. 4 B, E, H). These abnormalities, absent in HTZ muscle from 3-week-old mice

(Fig. S3), were also observed on modified gomori trichrome (GT), succinate dehydrogenase (SDH), cytochrome c oxidase (COX) and menadione-linked alpha-glycerophosphate dehydrogenase (Menad) stained sections (Fig. 4 C, F, I and Fig. S4), suggesting that both mitochondria, endoplasmic and sarcoplasmic reticulum could be affected. Based on staining intensities this remodeling was present in both oxidative and glycolytic fibers. A similar disorganization was found in *soleus* muscle mainly at 2 months (Fig. S5). There was no modification of glycogen or lipid, stained with periodic acid Schiff (PAS) and oil Red O (ORO) respectively, in TA and *soleus* muscles at the different ages tested (Fig. S3 and S4).

When compared to WT, the minimum fiber diameter was unchanged in HTZ TA muscle at 3 weeks (14.2 ± 1.2 µm in HTZ vs 16.3 ± 1.2 µm in WT), but a significant 14% decrease in fiber size was measured at 2 months of age (37.0 ± 1.5 µm vs 31.8 ± 0.9 µm), reaching 21% at 8 months (41.2 ± 0.9 µm vs 32.1 ± 1.6 µm). Muscle atrophy spared the fast fibers expressing the myosin heavy chain 2a (MHC-2a) and thus resulted from prominent atrophy of fast muscle fibers expressing the MHC-2b isoform (Fig. S6 A). In *soleus* muscle, fiber size was slightly reduced at 2 and 8 months of age even if statistical significance was not reached at 8 months (32.8 ± 1.3 µm vs 28.0 ± 1.1 µm $P < 0.05$; 40.3 ± 1.8 µm vs 35.3 ± 0.4 µm, $P = 0.06$ at 2 and 8 months, WT vs HTZ, respectively). For this mixed muscle, both slow expressing MHC-1 and fast fibers expressing MHC-2a equally contributed to muscle fiber size reduction (Fig. S6 B). By contrast to TA, muscle mass and fiber size in *soleus* increased between 2 and 8 months. In HTZ *soleus*, a significant 30% increase in total fiber number was observed at 2 and 8 months (554 ± 32 vs 719 ± 35, $P < 0.01$; 522 ± 31 vs 669 ± 21, $P < 0.05$ at 2 and 8 months, WT vs HTZ, respectively).

Electron microscopy analysis was performed on quadriceps muscles from mice at 2 and 8 months of age (Fig. 4 J-M). In HTZ mice, sarcomere organization and alignment, sarcoplasmic reticulum (SR) and T-tubules arrangement, morphology of mitochondria and

nucleus were preserved irrespectively of the age. However, a slight increase in intermyofibrillar and subsarcolemmal mitochondria content could be observed (Fig. 4 J, K). The myofibrils appeared smaller in HTZ muscle fibers and tubular structure density was increased in the intermyofibrillar space (Fig. 4 L, M).

Muscle weakness. Maximal force production was measured in TA and *soleus* muscles. At 3 weeks of age, absolute maximal force was decrease by about 40% in TA muscle (Table 1). This weakness took place without modification of muscle mass leading to a dramatic 40% reduction of specific maximal force at 2 and 8 months. Absolute maximal force reduction persisted in TA muscle whereas muscle atrophy had developed (20 and 25% mass loss at 2 and 8 mo, respectively). At both ages specific maximal force was reduced by 25% when compared to WT. Direct stimulation of the TA muscle and supra-maximal stimulation of the sciatic nerve gave the same result. Furthermore, no histomorphological abnormalities were detected in sciatic nerve of HTZ mice (Fig S7), suggesting a specific muscle involvement. For *soleus* muscle, absolute specific force was significantly decreased by 20% at 2 months and muscle mass was slightly increased. Muscle weight gain and muscle weakness were transient since they were not detected at 3 weeks nor at 8 months. *Soleus* muscle response to fatigue was also evaluated and no modification was observed (Table 1).

Subcellular localization of DNM2, [Ca^{2+}] measurements and dysferlin localization. The localization of Dnm2 in mouse skeletal muscle has so far never been characterized. However, despite multiple attempts, the commercially available DNM2 antibodies never gave satisfactory immunostaining on muscle sections. To circumvent this limitation, characterization of the expression pattern of Dnm2 was performed on isolated fibers from *Flexor digitorum brevis* (FDB) and interosseus muscles. In WT fibers, Dnm2

immunoreactivity was prominent at the periphery of the fibers where Dnm2 displayed a transversal striated pattern along the fiber in addition to perinuclear and longitudinal stainings (Fig. 5 left panel). There was no signal when primary antibody was omitted and a similar staining was obtained using two other anti-Dnm2 primary antibodies (15) (data not shown). The striated transversal staining pattern was centered on the Z-line labelled by α-actinin (Fig. 5 A-C) and laterally limited by the T-tubules markers dihydropyridine receptor (DHPR) (Fig. 5 D-F) and Amphiphysin 2 (not shown). These data indicate that Dnm2 entirely occupies the I-band. The longitudinal Dnm2 immunoreactivity co-localized with the longitudinal SR marker sarco/endoplasmic reticulum Ca^{2+}-ATPase (SERCA) (Fig. 5 J-L) and microtubules revealed by α-tubulin labelling (Fig. 5 G-I). In the perinuclear region, Dnm2 also co-localized with the microtubule network and with the microtubule organizing centre (MTOC) marker γ-tubulin (not shown). The cis-Golgi marker GM130 displayed a perinuclear and sarcoplasmic labelling at regions where the Dnm2 was also concentrated (Fig. 5 M-O). A Dnm2 accumulation was also found in the post-synaptic region of the neuromuscular junction characterized by α-bungarotoxin labelling (Fig. 5 P-R). Finally, DNM2 was found to co-localize with clathrin in the most peripheral part of the fibers including the perinuclear region (Fig. 5 S-U). In HTZ mice, the peripheral Dnm2 expression pattern was unchanged. In addition, α-tubulin, γ-tubulin and GM130 distribution were also unchanged in HTZ fibers (Fig. 6) as well as clathrin staining (not shown). The well-characterized double rows of triad dots corresponding to the DHPR (T-tubules marker) and RYR1 (SR marker) in WT fibers were slightly disorganized in HTZ fibers (Fig. 6). The central region of the WT and HTZ isolated fibers showed a weaker Dnm2 immunoreactivity when compared to peripheral subsarcolemmal area. Interestingly, after 48 hours maintenance in culture, Dnm2 large intracellular accumulations were observed for some HTZ fibers (Fig. 7 A). A three-dimensional reconstruction of the confocal image stacks in the xz and yz axes showed that

Dnm2-positive structures may cover a large portion of the fiber from the sarcolemma to the center of the fiber. These disorganized areas contained enlarged vesicular components surrounded by mitochondrial accumulation as evidenced by ultrastructural analysis (data not shown).

In order to assess potential Ca^{2+} homeostasis defects in the HTZ mice, we used the Fura-2 Ca^{2+} probe to measure the intracellular Ca^{2+} concentration. We found a significant increase in basal cytosolic Ca^{2+} concentration in HTZ isolated fibers from 3-month-old mice (95.9 ± 4.3 nM vs 172.9 ± 8.5 nM, $P < 0.05$; $n = 140$ fibers from 4 WT mice and $n = 113$ fibers from 2 HTZ mice). Given that the compartments responsible for Ca^{2+} homeostasis (T-tubules and SR) were only slightly disorganized, we tested if the intracellular Ca^{2+} increase could result from fragility of the sarcolemma using dysferlin immunostaining and plasma membrane staining using FM4-64 dye. We observed a normal sarcolemmal staining of dysferlin as well as normal staining of sarcolemmal and T-tubules membrane using FM4-64 in HTZ isolated fibers (Fig. 7 A and B). However, dysferlin intracellular accumulations occurred and co-localized with Dnm2 (Fig. 7 A) while no dysferlin labelling could be detected when the primary antibody was omitted. In this context human biopsies were tested for dysferlin localization (Fig. 8). In biopsies from DNM2-CNM patients harboring 4 different mutations, in addition to the normal sarcolemmal staining, an abnormal intracytoplasmic staining was found when compared to biopsy from a healthy control subject. In contrast, there is no or faint cytoplasmic staining on muscle biopsies from DNM2-CMT and MTM1-CNM patients, and in one genetically unresolved case of CNM without *DNM2* mutation.

Muscle phenotype in homozygous mouse. Only 6 HMZ mice survived after birth and grew with pronounced growth retardation (30% of body weight reduction compared to WT and

HTZ littermates at 3 weeks). Five mice died at weaning and one was sacrified before death in order to perform histomorphological and ultrastructural analyses. The angular shape of muscle fibers was barely preserved but presented enlarged connective tissue. However, no sign of regeneration was observed (Fig. 9 A, D). Fiber size was homogenous but strongly reduced when compared to WT littermates (37% decrease). Myonuclei were internalized in 10% of fibers and centralized in 2%. Intermyofibrillar disorganizations were observed with NADH-TR, GT, SDH, COX and Menad stainings (Fig. 9 B, C, E, F). In addition to the staining accumulation centered in the middle as reported in the HTZ mice, pale areas devoid of oxidative enzymes activity, disorientation of the intermyofibrillar network were also observed. Other histochemical staining procedures did not reveal additional abnormalities. Using electron microscopy, we detect an increase in the connective tissue, evident when compared to WT (Fig. 9 G, H). On longitudinal sections, regular organization of myofibrils was lost and dilation as well as proliferation of tubular structures especially in the Z-line vicinity were detected (Fig. 9 I, J). Furthermore, irregularity of Z and M-bands and some internalized nuclei could be observed (Fig. 9 K, L).

Phenotype in mouse embryonic fibroblasts. Because of the neonatal lethality, mouse embryonic fibroblasts (MEFs) were cultured in order to have access to HMZ cells. The normal Dnm2 expression was assessed by RT-PCR (Fig. 10 A) and western-blot analysis (Fig. 10 B) in the 3 genotypes. In addition to Dnm2, MEFs express Dnm1 mRNA and also Dnm3 but at low level (Fig. 10 A). Immunocytochemistry showed no change in subcellular localization of Dnm2 in HTZ and HMZ MEFs compared to WT fibroblasts (Fig. 10 C). Integrity of both microtubule and actin networks was also preserved (Fig. 10 C). The clathrin-mediated endocytosis was tested in MEFs from the 3 genotypes using a fluorescent-transferrin uptake assay (Fig. 10 D). Quantification of the transferrin-associated signal showed that WT

and HTZ MEFs were capable of internalizing equal amounts of fluorescent transferrin but pointed out to a significant decrease in transferrin uptake in HMZ MEFs.

Discussion.

Human DNM2-CNM is defined by muscle weakness, characteristic histopathological changes and absence of dystrophic process or inflammation (6). To date no curative treatment is available and the pathophysiological mechanisms are still largely unknown. In this context, development of animal models mimicking the human condition is an important step. In the current work, we have characterized the first *in vivo* model of DNM2-linked myopathy, i.e. the KI-*Dnm2*^{R465W} mouse, expressing the most frequent CNM-related *DNM2* mutation.

In HTZ mice, the earliest alteration detected was the reduction in force generation affecting the TA muscle at 3 weeks of age in absence of muscle mass modification, fiber size or histomorphological alterations. Muscle atrophy was observed at 2-month-old and morphological alterations became visible (see below). Similarly, in the neonatal DNM2-CNM, generalized hypotonia and muscle weakness precede histological abnormalities since the characteristic radiating sarcoplasmic strands are mostly absent in these patients (3, 9). Altogether, these results suggest that expression of the DNM2 mutant impairs the quality of contraction. Subsequently, fiber size reduction and myofibrillar disorganization can contribute to persistence of muscle weakness at later ages. *DNM2* mutations were identified in the peripheral nerve Charcot-Marie-Tooth disease (7, 8) and we have shown that DNM2 is a component of the neuromuscular junction's post-synaptic compartment. In our experiments, when all the motor units were stimulated by supra-maximal sciatic nerve stimulation, the decrease in force generation was identical to direct muscle stimulation response. These results suggest a specific muscle affection where neurotransmission and nerve condution were spared as reported in human patients harboring 3 differents mutations in the middle domain of the protein, including the p.R465W mutation (4). However, electrophysiological exploration

(nerve conduction velocity studies and electromyogram) will be necessary to exclude nerve involvement in this model.

Maintenance of skeletal muscle mass critically depends on the balance between protein synthesis and degradation (16). During phases of muscle wasting such as disuse, denervation or through various disease states, expression of numerous genes is modulated (17, 18). The ubiquitin-proteasome and the autophagy-lysosome systems are two degradation pathways that could accelerate protein breakdown over protein synthesis (19). The transcription factor FOXO3a is a common regulator of the two pathways particularly important for regulation of the expression of the atrogenes, MuRF1 and Atrogin1 (20, 21), and the autophagy-related genes, LC3 and Gabarapl1 (22). In our study, FOXO3a-dependent signaling activation, observed both at transcriptional and cellular levels, was associated to a transient increase of MuRF1 and Gabarapl1 at 2 months of age. At 8 months, up-regulation of MuRF1 and Gababarpl1 was no longer observed and all values returned to basal level. This strongly suggests that an acute atrophy process is triggered between weaning and the first 2 months. Furthermore, between 2 and 8 months neither TA muscle mass nor fiber size increased suggesting that growth arrest occurred in this muscle. Increased basal Ca^{2+} level in our model could also contribute to activation of the ubiquitin-proteasome system since the initial step for actomyosin degradation requires activation of Ca^{2+} sensitive calpains (23) and/or caspases (24). Expression of these atrophy-related genes was tested in 2 adult patients harboring a mutation in the middle domain. FOXO3a and Gabarapl1 were found to be increased only in one patient. Further study including more patients and especially younger patients (with neonatal and childhood onsets) will be necessary to determine the relevance of these data in the DNM2-related atrophy occurring in CNM patients.

Histopathological and ultrastructural analyses in HTZ mice showed that sarcolemma and sarcomere integrity were preserved. Intermyofibrillar disorganization, mainly affecting

mitochondria and reticulum distribution, was closely related to the radial distribution of sarcomeric strands reported for human pathology. In TA muscle from the unique HMZ mouse studied, morphological abnormalities were accentuated when compared to HTZ mice, and pronounced fiber size reduction was present as soon as 3 weeks of age. The unexpected result is the absence of nuclear centralization in HTZ mice, even at 2 years of age in this model of DNM2-linked myopathy. Nuclear internalization does occur in the HMZ mouse but at a relatively low level (10%) in comparison to the proportion seen in patients (up to 90% of fibers have central nuclei). The molecular mechanisms which control the nuclear positioning in muscle fibres are not well understood and mechanistic understanding of the DNM2 involvement in this process is still largely unknown. We can hypothesize from our results that *DNM2* mutation affects both contractile properties and nuclear positioning independently and that in mice the nuclear positioning processes are less sensitive to DNM2 dysfunction. Alteration of these processes becomes observable when a severe DNM2 dysfunction is reached with homozygous mutation. Cultured myoblasts and myotubes from HMZ neonates will be extremely useful to clarify Dnm2 involvement in nuclear positioning.

Muscle atrophy progressed spatially with age since *gastrocnemius/plantaris* and quadriceps muscle mass loss became significant at 8 months. However, all muscles do not behave similarly since the two more oxidative muscles in mouse, diaphragm and *soleus*, exhibit a slight and transient hypertrophy at 2 months of age. *Soleus* behavior is of particular interest at 2 months i.e. when TA muscle is becoming weaker. Associated to a generalized hypotrophy of muscle fibers, we observed hyperplasia and histological abnormalities. Predominance and atrophy of slow muscle fibers was not observed in contrast to the human DNM2-CNM. However, relative to fiber type, the *Dnm2* mutation has a specific impact in mice with prominent atrophy of fast MHC-2b expressing fibers in TA muscle. Further investigations are required to understand such spatial and temporal muscle involvement due to

a *DNM2* mutation which is also described in the human disease where distal involvement precedes proximal muscle affection (4, 5).

To understand how *DNM2* mutation can induce a muscular phenotype, a crucial question was to characterize the subcellular localization of the protein in skeletal muscle. In this work, we report that Dnm2 localizes predominantly at the I-band and perinuclear regions, two regions of intense membrane trafficking in muscle (25). In addition, DNM2 also partially co-localizes with the microtubule network especially in the perinuclear region, which includes the MTOC (26, 27). Altogether, these data suggest that, DNM2 could be involved in a wide range of cellular processes in skeletal muscle. Among them, possible defects in the MTOC function, microtubule organization and clathrin-mediated processes have been already established in cells transfected with various DNM2 mutants (2, 8, 13, 14). However, clathrin-mediated endocytosis assays performed in MEFs showed impairment only in HMZ cells. Given the subcellular Dnm2 localization reported here, a dominant negative effect of the *Dnm2* mutant on intracellular membrane trafficking or on cytoskeleton regulation may participate to the pathomechanisms in our Knock-in mouse model. This can occur through the formation of abnormally stable Dnm2 polymers that fail to disassemble under addition of GTP as recently reported for four CNM-*DNM2* mutations, including the p.R465W mutation (28)

Several findings obtained from studies on animal models of CNM associated with mutations in myotubularin (MTM1) or amphiphysin 2 (BIN1) raised the possibility that CNM could result from a dysfunction of the T-tubules system. Indeed, the muscle specific isoform of amphiphysin 2 is concentrated at T-tubules and was shown to be involved in their organization (29, 30). Myotubularin is also located to the T-tubules (31, 32) and knock-down of myotubularin leads to disorganization of the T-tubules system and defects in excitation-contraction coupling (32, 33). Our electron microscopy analysis and immunocytochemical

detection of DHPR, amphiphysin 2, and RyR1 on isolated muscle fibers suggest that the triad structure (T-tubules and the SR terminal cisternae) was not significantly affected in our model. Nevertheless, an elevated cytosolic Ca^{2+} concentration was clearly observed. The partial co-localization of Dnm2 with SERCA, a Ca^{2+}-ATPase which pumps Ca^{2+} from the cytosol back to the lumen of the SR, may suggest involvement of this Ca^{2+} storage compartment in the intracellular Ca^{2+} increase. On the other hand, elevated basal Ca^{2+} may also result from a Ca^{2+} influx due to sarcolemma fragility but the precise molecular mechanism needs to be further investigated.

In HTZ isolated muscle fibers, we evidenced an abnormal cytoplasmic retention of DNM2 and dysferlin in well-delimited area. We can hypothesize that these large intracellular accumulations result from a defect of DNM2-dependent trafficking which remains to be explored. Dysferlin acts in Ca^{2+}-dependent membrane repair process (34) but the plasma membrane integrity appears unaffected in basal conditions in HTZ muscle fibers. Further studies will be necessary to assess the dysferlin-dependent membrane repair after injury to specify the relevance of dysferlin retention in the pathomechanisms occurring in the KI-*Dnm2*^{R465W} mice. Interestingly, an intracellular accumulation of dysferlin was also identified in biopsies from DNM2-CNM patients but not in DNM2-CMT nor MTM1-CNM patients. Cytoplasmic retention was already reported in some cases of muscular dystrophy due to caveolin 3 mutations (35, 36) but so far, never reported in congenital myopathies. Other sarcolemmal markers (α-sarcoglycan, β-dystroglycan, and caveolin 3) exhibited normal staining in the same DNM2-CNM biopsies (data not shown). Dysferlin staining in other forms of CNM linked to BIN1, RYR1, or MTMR14 will be required to establish dysferlin staining as a novel marker of DNM2-CNM biopsies and thus orientate direct genetic testing.

MEFs in primary culture allowed the study of HMZ cells and showed a 30% decrease in transferrin uptake, a marker of the clathrin-mediated receptor endocytosis. This can reflect the

incomplete loss-of-function of the DNM2 and/or the participation of DNM1 expressed in these cells (37). We can hypothesize that the neonatal lethality results from an important and generalized defect of clathrin- and Dnm2-dependent membrane trafficking. Knock-out mouse models for the two clathrin adaptor proteins adaptor-related protein complexes AP1 and AP2 induced an early embryonic lethality (38, 39) and more recently, a knock-out model for Dnm2 was shown to be lethal at embryonic days E8-E12 (37). A knock-out model for the neuronal Dnm1 was also lethal within 2 weeks because of a severe impairment of synaptic vesicle endocytosis (40). Such endocytosis impairment could affect homeostasis of several physiological systems crucial for neonatal survival through mechanisms which remain to be elucidated. This may include alteration of fluid-electrolyte balance or energy metabolism (41). Nevertheless, our results suggest that the HMZ p.R465W mutation is associated with an important but incomplete loss-of-function of Dnm2, allowing intrauterine development, but incompatible with life after birth.

In conclusion, we have shown that expression of the mutated Dnm2 in KI-*Dnm2*^{R465W} mouse model has early muscle defects, progressive atrophy, and morphological abnormalities similar to those observed in human biopsies. The HTZ mice, can be considered as the first animal model of dominant congenital myopathy due to *Dnm2* mutation. Availability of this *in vivo* model of DNM2-myopathy, developing a muscle-specific phenotype at the HTZ will be helpful to broaden our understanding of the disease and to investigate future therapeutic strategies. Finally, the current model will also be a precious tool to better define the *in vivo* functions of DNM2 in skeletal muscle.

Material and Methods.

Production of KI-*Dnm2*^{R465W} mice. The dynamin 2 mutant mouse line was established at the Mouse Clinical Institute (MCI, Illkirch, France; http://www-mci.u-strasbg.fr). The targeting vector was constructed as follows. A 439 bp fragment encompassing dynamin 2 intron 10, exon 11 (87 bp) and intron 11 was amplified by PCR (from 129S2/SvPas genomic DNA) in two steps to allow the introduction of the point mutation A>T in exon 11 (arginine changed to tryptophan) and subcloned in an MCI proprietary vector, resulting in step1 plasmid (Fig. 1 A). This MCI vector has a floxed neomycin resistance cassette. A 5.2 kb fragment (5' homology arm) and a 3.4 kb fragment (3' homology arm) were amplified by PCR and subcloned successively in step1 plasmid to generate the final targeting construct. The linearized construct was electroporated in 129S2/SvPas mouse embryonic stem cells. Targeted clones were identified by PCR using external primers and further confirmed by Southern blot with 5' and 3' external probes. One positive embryonic stem cell clone was injected into C57BL/6J blastocysts, and male chimaeras derived gave germline transmission. Genotyping was performed by PCR on DNA extracted from tails using the forward (F) primer 3'-CTGCGAGAGGAGACCGAGC-5' in the exon 11 and the reverse (R) primer 3'-GCTGAGCACTGGAGAGTGTATGG-5' in the intron 11 (Fig. 1 A, B). Molecular, histological and functional phenotypes were characterized in HTZ male mice and their sex-matched wild-type littermate at 3 weeks (weaning group), 2 and 8 months of age. Mice were sacrified by cervical dislocation under isoflurane anesthesia. Neonates were used in specified studies and were sacrificed by decapitation during the first day of life. All animal studies were performed in compliance with the French guidelines.

Locomotion tests. The exploratory locomotion of mice was examined in an openfield test. Mice were placed on a 40 cm x 40 cm area and locomotion duration was measured for 10 min. For endurance exercise performance, mice were acclimated to moderate intensity running (5-20 cm/s for 20 min per day) on a motorized treadmill (0% incline) during 3 consecutive days before the endurance test. During the first 15 min of the endurance test, speed was increase from 5 to 15 cm/s (warm up). In the following 5 min speed was increased from 15 cm/s to 35 cm/s and then maintained constant until exhaustion, defined as an inability to run despite repeated contact with the electric grid. Endurance exercise performance was estimated from the duration (min) of the run at 35 cm/s.

Total RNA extraction and cDNA analysis. Tissue samples were snap frozen in liquid nitrogen and powdered when weight exceeded 30 mg, otherwise samples were directly resuspended in the extraction buffer. RNA extraction was performed using RNeasy fibrous tissue (Qiagen). Total RNA from cultured cells was extracted using trizol reagent (Invitrogen). Total RNA (500 ng) was submitted to reverse transcription using the Superscript II reverse transcriptase kit (Invitrogen). PCRs were realized with Platinum Taq polymerase (Invitrogen) following manufacturer's instructions. The Dnm2-forward primer was designed to target exon 10 (5'-GGTGGTCAAGCTGAAAGAGC-3') and the reverse primer was designed to target exon 14 (5'-GCTGTCAGCACGAACCAGTA-3'). RT-PCR products were purified and sequenced using ABI PRISM BigDye Terminator cycle sequencing ready reactions kit 3.1 on a 377 Genetic Analyzer (Applied Biosystems). For amplification of Dnm1 and Dnm3 transcripts, the forward and reverse primers were: 5'-AGATGGAGCGAATTGTGACC-3' and 5'-GAATGACCTGGTTCCCTGAA-3' for Dnm1, 5'-ATGCTCCGAATGTACCAAGC-3' and 5'-GAGGGGAGCACTTATCGTCA-3' for Dnm3. Quantification was performed using the following forward and reverse primers: 5'-ACCCCACACTTGCAGAAAAC-3' and

5’-GCCTTCTCAAAGTCCACTCC-3’ for Dnm2, 5’-TCGTGCTCTGAACTCCTTG-3’and 5’-TGGAGTGTCTGGTTGCCGT-3’for FOXO3a, 5’-GCCTTCAAAGGCCTCACG-3’ and 5’-CTGAGCACATGCAGGTCTGGG-3’ for Atrogin1, 5’-CGACCGAGTGCAGACGATCATCTC-3’ and 5’-GTGTCAAACTTCTGACTCAGC-3’ for MuRF1, 5’-CGTCCTGGACAAGACCAGT-3’and 5’-ATTGCTGTCCCGAATGTCTC-3’ for LC3, 5’-CATCGTGGAGAAGGCTCCTA-3’ and 5’-ATACAGCTGGCCCATGGTAG-3’ for Gabarapl1, on a LightCycler480 System using the LighCycler480 SYBR Green I Master mix (Roche Applied Science). The program included an initial denaturation step of 10 min at 95°C, followed by 40 amplification cycles of denaturation at 95°C for 15 sec, annealing at 62°C for 30 sec, and elongation at 72°C for 15 sec. For normalization purposes, amplification of the housekeeping gene encoding the acidic ribosomal phosphoprotein P0 (Arbp), was performed on the same plate (forward primer: 5’-CTCCAAGCAGATGCAGCAGA-3’; reverse primer: 5’-ATAGCCTTGCGCATCATGGT-3’). Data were analyzed with the LightCycler480 software (Roche Applied Science).

Histomorphological and ultrastructural analyses. Samples were frozen in liquid nitrogen-cooled isopentane. Transverse sections of TA muscle (8 µm thick) were stained with hematoxylin and eosin (HE), modified gomori trichrome (GT), oil red O (ORO), periodic acid schiff (PAS), reduced nicotinamide adenine dinucleotide-tetrazolium reductase (NADH-TR), cytochrome c oxidase (COX), succinate dehydrogenase (SDH) and menadione-linked α-glycerophosphate dehydrogenase (Menad) stains by standard methods (42). Light microscopy were performed using an upright microscope (DMR, Leica) and 40× NA 0.85 HCX Plan Apo objective (Leica). Images were captured using a monochrome camera (DS-Ri1, Nikon) and NIS-Elements BR software (Nikon). For all imaging, exposure settings were identical between compared samples and viewed at room temperature. Fiber size was determined on

TA muscle sections immunocytochemically labelled with laminin and with different MHC isoforms as previously described (44). For electron microscopy, muscles were fixed with 2.5% paraformaldehyde, 2.5% glutaraldehyde in 50 mM $CaCl_2$, 0.15 M cacodylate buffer (pH 7.4). Samples were postfixed with 2% OsO_4, 0.8% $K_3Fe(CN)_6$ in 0.15 M cacodylate buffer (pH 7.4) for 1 h at 4 °C and incubated with 5% uranyl acetate for 2 h at 4 °C. Muscles were dehydrated in a graded series of ethanol and embedded in epon resin. Thin (70 nm) sections were stained with uranyl acetate and lead citrate and observed using a Philips CM120 electron microscope (Philips Electronics NV).

Muscle contractile properties. The isometric contractile properties of TA muscles were studied *in situ* on mice anesthetized with 60 mg/kg pentobarbital. The distal tendon of the TA muscle was attached to a lever arm of a servomotor system (305B Dual-Mode Lever, Aurora Scientific). The sciatic nerve was stimulated by a bipolar silver electrode using a supramaximal (10 V) square wave pulse of 0.1 ms duration. Muscles were also directly stimulated (80 V). Absolute maximal isometric tetanic force (P_0) was measured during isometric contractions in response to electrical stimulation (frequency of 25–150 Hz; train of stimulation of 500 ms). All isometric contraction measurements were made at optimal muscle length (L_0) at which P_0 was obtained. TA muscles were weighted and specific force (sP_0) was calculated by dividing P_0 by muscle weight. The isometric contractile properties of *soleus* muscles were studied *in vitro*. Mice were euthanized after the removal of *soleus* muscles. *Soleus* muscles were soaked in an oxygenated Krebs solution (95% O_2 and 5% CO_2) containing 58.5 mM NaCl, 24 mM $NaHCO_3$, 5.4 mM KCl, 1.2 mM KH_2PO_4, 1.8 mM $CaCl_2$, 1 mM $MgSO_4$, and 10 mM glucose, pH 7.4 at 22°C. One of the muscle tendons was attached to a lever arm of a servomotor system (300B Dual-Mode Lever, Aurora Scientific). After equilibration (30 min), electrical stimulation was delivered through electrodes running parallel

to the muscle. One ms pulses were generated by a high power stimulator (701B, Aurora Scientific). P_0 was measured at L_0 during isometric contractions in response to electrical stimulation (frequency of 50–125 Hz; train of stimulation of 1500 ms). Fatigue resistance was determined after a 5 min rest period. The muscles were stimulated at 75 Hz during 500 ms every 1.6 s for 3 min. The time taken for initial force to fall by 30% (F30%) was determined. *Soleus* muscles were weighted and specific maximum tetanic force (sP_0) was calculated by dividing P_0 by the estimated cross-sectional area of the muscle. Assuming muscles have a cylindrical shape and a density of 1.06 mg/mm^3, the cross-sectional area corresponds to the volume of the muscle divided by Lf. The Lf to L0 ratio of 0.70 was used to calculate Lf.

Mouse embryonic fibroblasts (MEFs) and isolated muscle fibers. Experiments were performed on MEFs in primary cultures, i.e. 1 or 2 passages after dissection of E13.5 days embryos. Cells were cultured at 37°C (5% CO_2) in Dulbecco's modified Eagle's medium (DMEM) containing 10% fetal calf serum (FCS) supplemented with penicillin, streptomycin, L-glutamate, and sodium pyruvate. For the transferrin uptake assay, MEFs were cultured in DMEM without FCS at 37°C for 45 min. Transferrin-AlexaFluor555 (Invitrogen) was added at 20 µg/ml at 37°C for 15 min. Cells were washed 3 times with PBS and fixed in 4% paraformaldehyde before analysis using a confocal microscope Leica SP2. The transferrin-associated signal was quantified using ImageJ software (NIH; http://rsbweb.nih.gov/ij). FDB and interosseous muscles were dissected from 2 to 7-month-old WT and HTZ male mice and digested for 2 hours in 2.5 mg/ml Worthington's collagenase type 2 under agitation at 37°C. Fibers were dissociated by gentle trituration before seeding on coverslips coated with matrigel (BD Biosciences). Immunocytochemistry was performed after 24 to 48 hours in DMEM supplemented with 2% horse serum. For the cytosolic [Ca^{2+}] measurements at rest, freshly isolated fibers were plated on laminin-coated coverslips. Plated fibers were loaded by

exposure to 5 µM of the Ca^{2+} fluorescent dye fura 2-AM (Invitrogen). Ratiometric fura-2 fluorescence measurements were made with an integrated IonOptix device (IonOptix). The cytosolic [Ca^{2+}] was calculated from ratiometric measurements according to a modified method from Grynkiewicz et al. (44, 45). Membrane staining was achieved by 1 min incubation on ice with FM4-64FX dye (Invitrogen, France) at 5µg/ml in cold HBSS buffer (Invitrogen) and fixation 10 min in 4% paraformaldehyde.

Protein extraction and western blot analysis. Muscles and cells were lysed in a 10-fold dilution (w/v) of buffer containing 150 mM NaCl, 50 mM Tris pH 7.2, 1 mM EDTA, 0.1% Triton X100, 10% glycerol, 5 mM $MgCl_2$, 1% phosphatase inhibitor cocktail 1 and 2 (P2850 and P5726 from Sigma-Aldrich) and 1% protease inhibitor cocktail (P8340 from Sigma-Aldrich) by sonication (3 x 5 s). Samples were agitated for 20 min at 4°C then centrifugated at 15,000 g at 4°C for 10 min. Supernatants were collected and protein concentrations were determined with the BCA Protein Assay kit (Thermo Scientific). Forty micrograms of total proteins in loading buffer (50 mM Tris-HCl, 2% SDS, 10% glycerol, 1% β-mercaptoethanol and bromophenol blue) were loaded on 7.5% SDS-PAGE for electrophoretic separation, transferred on polyvinylidene fluoride (PVDF) membrane for 1.5 h at 300 mA at 4°C. Membranes were blocked for 1 h in PBS containing 5% non fat dry milk and 0.1% Tween20 before an overnight incubation with primary antibodies against DNM2 (Santa-Cruz SC-6400, 1:400), α-tubulin (Sigma-Aldrich T5168, 1:1000) and vinculin (Sigma-Aldrich V9131, 1:1000) diluted in blocking buffer containing 1% milk. Incubation with horseradish peroxidase-conjugated antibodies (anti-goat, anti-mouse or anti-rabbit from Dako) was performed for chemiluminescence detection using the Supersignal West Pico Chemiluminescent kit (Pierce). Acquisition was performed on G-Box (Ozyme) and quantitative analyses were realized with GeneTools software (Syngene).

Immunocytochemistry. MEFs, isolated fibers and muscle sections were fixed 15 min at room temperature in paraformaldehyde 4%. Non specific sites were blocked in PBS-2% horse serum - 0.5% IgG free BSA-0.1% Triton X-100 for 90 min and incubated overnight with the primary antibodies diluted in blocking buffer. The isolated muscle fibers were additionally permeabilized 10 min by 0.1% Triton X-100 in PBS before saturation of unspecific sites. Following antibodies were used: DNM2 (Abcam, ab52269), α-tubulin (Sigma-Aldrich, T5168), γ-tubulin (Santa-Cruz, sc-17787), SERCA1/2 (Novocastra, mouse monoclonal NCL-SERCA1 and NCL-SERCA2), GM130 (BD Biosciences, 610823), α-actinin (Sigma-Aldrich, A7811), DHPRα1 (Abcam, ab58552), RYR1 (Sigma-Aldrich, R129), FOXO3a (Cell Signaling Technology, 2497). Rabbit polyclonal anti-BIN1 antibody was a gift from Dr Jocelyn Laporte (IGBMC, Illkirch, France). Mouse monoclonal X22 anti-clathrin CHC17 was provided by Pr. Frances Brodsky (UCLA, San Fransisco, USA). For DNM2 immunostaining in FDB muscle fibers, 2 other DNM2 antibodies were used: anti-DNM2 (BD Transduction Laboratories, 610264) and a rabbit polyclonal anti-DNM2 antibody provided by Mark McNiven (Mayo Clinic, Rochester, USA). After washing, immunostaining was revealed by incubation for 2 h with AlexaFluor488- or AlexaFluor568-conjugated anti-rabbit or anti-mouse antibodies (Invitrogen) diluted at 1:400. Actin fibers were labelled using AlexaFluor568-phalloidin (Invitrogen) following the manufacturer's instructions. Neuromuscular junctions were labelled with α-bungarotoxin (Invitrogen, A1175). Labelled MEFs and muscle sections were visualized by fluorescence microscopy using upright microscope (Axiophot2; Carl Zeiss) and 40× NA 1.30 Plan NeoFluar objectives (Carl Zeiss). Images were captured using a charge-coupled device monochrome camera (Coolsnap fx Photometric) and MetaMorph software. For all imaging, exposure settings were identical between compared samples and viewed at room temperature. Isolated fibers were mounted in

Vectashield hard-set containing DAPI (Vector Laboratories) before imaging using a confocal acquisition performed using a spectral confocal laser-scanning microscope (SP2 AOBS; Leica) on an inverted microscope (Leica). Confocal software (LCS; Leica) was used for acquisition with a Plan Apo 63× NA 1.4 oil objective (Leica). For all imaging, exposure settings were identical between compared samples and viewed at room temperature.

Statistics

Data are means ± SEM. The number of samples is specified in all figure legends. Statistical comparisons were performed using a Mann-Whitney *U*-test for all experiments except for cytosolic Ca^{2+} measurements and transferrin uptake assay where an unpaired Student's *t*-test was performed. For HTZ to WT comparison the 0.05 level of confidence was accepted for statistical significance.

Acknowledgements.

We thank the Plateforme d'Imagerie de la Pitié Salpétrière for confocal imaging acquisition facilities. Perrine Castets, Valérie Allamand and Damien Freyssenet are acknowledged for the fruitful discussions.

Conflict of Interest statement. None declared.

Funding

This work was supported by the Institut National de la Santé et de la Recherche Médicale (Inserm), Institut de Myologie (AIM), the Association Française contre les Myopathies (AFM), Université Pierre et Marie Curie-Paris6 (UPMC) and the Centre National de la Recherche Scientifique (CNRS). ACD was the recipient of a fellowship from the Région Ile-de-France and Association Institut de Myologie (AIM). AV and BF were recipients of AIM fellowships and SV was the recipient of a UPMC-Emergence2009 fellowship.

References.

1. Jungbluth, H., Wallgren-Pettersson, C. and Laporte, J. (2008) Centronuclear (myotubular) myopathy. *Orphanet J. Rare Dis.,* **3,** 26.
2. Bitoun, M., Maugenre, S., Jeannet, P.Y., Lacene, E., Ferrer, X., Laforet, P., Martin, J.J., Laporte, J., Lochmuller, H., Beggs, A.H. *et al.* (2005) Mutations in dynamin 2 cause dominant centronuclear myopathy. *Nat. Genet.,* **37,** 1207-1209.
3. Bitoun, M., Bevilacqua, J.A., Prudhon, B., Maugenre, S., Taratuto, A.L., Monges, S., Lubieniecki, F., Cances, C., Uro-Coste, E., Mayer, M. *et al.* (2007) Dynamin 2 mutations cause sporadic centronuclear myopathy with neonatal onset. *Ann. Neurol.,* **62,** 666-670.
4. Fischer, D., Herasse, M., Bitoun, M., Barragan-Campos, H.M., Chiras, J., Laforet, P., Fardeau, M., Eymard, B., Guicheney, P. and Romero, N.B. (2006) Characterization of the muscle involvement in dynamin 2-related centronuclear myopathy. *Brain,* **129,** 1463-1469.
5. Schessl, J., Medne, L., Hu, Y., Zou, Y., Brown, M.J., Huse, J.T., Torigian, D.A., Jungbluth, H., Goebel, H.H. and Bonnemann, C.G. (2007) MRI in DNM2-related centronuclear myopathy: evidence for highly selective muscle involvement. *Neuromuscul. Disord.*, **17,** 28-32.
6. Romero, N.B. (2010) Centronuclear myopathies: a widening concept. *Neuromuscul. Disord.,* **20,** 223-228.
7. Fabrizi, G.M., Ferrarini, M., Cavallaro, T., Cabrini, I., Cerini, R., Bertolasi, L. and Rizzuto, N. (2007) Two novel mutations in dynamin-2 cause axonal Charcot-Marie-Tooth disease. *Neurology*, **69,** 291-295.

8. Züchner, S., Noureddine, M., Kennerson, M., Verhoeven, K., Claeys, K., De Jonghe, P., Merory, J., Oliveira, S.A., Speer, M.C., Stenger, J.E. *et al.* (2005) Mutations in the pleckstrin homology domain of dynamin 2 cause dominant intermediate Charcot-Marie-Tooth disease. *Nat. Genet.,* **37,** 289-294.

9. Susman, R.D., Quijano-Roy, S., Yang, N., Webster, R., Clarke, N.F., Dowling, J., Kennerson, M., Nicholson, G., Biancalana, V., Ilkovski, B. *et al.* (2010) Expanding the clinical, pathological and MRI phenotype of DNM2-related centronuclear myopathy. *Neuromuscul. Disord.,* **20,** 229-237.

10. Cook, T.A., Urrutia, R. and McNiven, M.A. (1994) Identification of dynamin 2, an isoform ubiquitously expressed in rat tissues. *Proc. Natl. Acad. Sci. U S A,* **91,** 644-648.

11. Praefcke, G.J. and McMahon, H.T. (2004) The dynamin superfamily: universal membrane tubulation and fission molecules? *Nat. Rev. Mol. Cell Biol.,* **5,** 133-147.

12. Durieux, A.C., Prudhon, B., Guicheney, P. and Bitoun, M. (2010) Dynamin 2 and human diseases. *J. Mol. Med.,* **88,** 339-350.

13. Bitoun, M., Durieux, A.C., Prudhon, B., Bevilacqua, J.A., Herledan, A., Sakanyan, V., Urtizberea, A., Cartier, L., Romero, N.B. and Guicheney, P. (2009) Dynamin 2 mutations associated with human diseases impair clathrin-mediated receptor endocytosis. *Hum. Mutat.,* **30,** 1419-1427.

14. Tanabe, K. and Takei, K. (2009) Dynamic instability of microtubules requires dynamin 2 and is impaired in a Charcot-Marie-Tooth mutant. *J. Cell Biol.,* **185,** 939-48.

15. Henley, J.R., Krueger, E.W., Oswald, B.J. and McNiven, M.A. (1998) Dynamin-mediated internalization of caveolae. *J. Cell Biol.,* **141,** 85-99.

16. Glass, D.J. (2003) Molecular mechanisms modulating muscle mass. *Trends Mol. Med.*, **9,** 344-350.

17. Lecker, S.H., Jagoe, R.T., Gilbert, A., Gomes, M., Baracos, V., Bailey, J., Price, S.R., Mitch, W.E. and Goldberg, A.L. (2004) Multiple types of skeletal muscle atrophy involve a common program of changes in gene expression. *FASEB J.*, **18,** 39-51.

18. Sacheck, J.M., Hyatt, J.P., Raffaello, A., Jagoe, R.T., Roy, R.R., Edgerton, V.R., Lecker, S.H. and Goldberg, A.L. (2007) Rapid disuse and denervation atrophy involve transcriptional changes similar to those of muscle wasting during systemic diseases. *FASEB J.*, **21,** 140-155.

19. Sandri, M. (2008) Signaling in muscle atrophy and hypertrophy. *Physiology (Bethesda),* **23,** 160-170.

20. Bodine, S.C., Latres, E., Baumhueter, S., Lai, V.K., Nunez, L., Clarke, B.A., Poueymirou, W.T., Panaro, F.J., Na, E., Dharmarajan, K. *et al.* (2001) Identification of ubiquitin ligases required for skeletal muscle atrophy. *Science,* **294,** 1704-1708.

21. Sandri, M., Sandri, C., Gilbert, A., Skurk, C., Calabria, E., Picard, A., Walsh, K., Schiaffino, S., Lecker, S.H. and Goldberg, A.L. (2004) Foxo transcription factors induce the atrophy-related ubiquitin ligase atrogin-1 and cause skeletal muscle atrophy. *Cell,* **117,** 399-412.

22. Zhao, J., Brault, J.J., Schild, A., Cao, P., Sandri, M., Schiaffino, S., Lecker, S.H. and Goldberg, A.L. (2007) FoxO3 coordinately activates protein degradation by the autophagic/lysosomal and proteasomal pathways in atrophying muscle cells. *Cell Metab.*, **6,** 472-483.

23. Kramerova, I., Kudryashova, E., Venkatraman, G. and Spencer, M.J. (2005) Calpain 3 participates in sarcomere remodeling by acting upstream of the ubiquitin-proteasome pathway. *Hum. Mol. Genet.*, **14,** 2125-2134.

24. Du, J., Wang, X., Miereles, C., Bailey, J.L., Debigare, R., Zheng, B., Price, S.R. and Mitch, W.E. (2004) Activation of caspase-3 is an initial step triggering accelerated muscle proteolysis in catabolic conditions. *J. Clin. Invest.,* **113,** 115-23.

25. Towler, M.C., Kaufman, S.J. and Brodsky, F.M. (2004) Membrane traffic in skeletal muscle. *Traffic,* **5,** 129-139.

26. Bugnard, E., Zaal, K.J. and Ralston, E. (2005) Reorganization of microtubule nucleation during muscle differentiation. *Cell Motil. Cytoskeleton,* **60,** 1-13.

27. Tassin, A.M., Maro, B. and Bornens, M. (1985) Fate of microtubule-organizing centers during myogenesis in vitro. *J. Cell Biol.,* **100,** 35-46.

28. Wang, L., Barylko, B., Byers, C., Ross, J.A., Jameson, D.M. and Albanesi, J.P. (2010) Dynamin 2 mutants linked to centronuclear myopathies form abnormally stable polymers. *J. Biol. Chem.,* **285,** 22753-22757.

29. Lee, E., Marcucci, M., Daniell, L., Pypaert, M., Weisz, O.A., Ochoa, G.C., Farsad, K., Wenk, M.R. and De Camilli, P. (2002) Amphiphysin 2 (Bin1) and T-tubule biogenesis in muscle. *Science,* **297,** 1193-1196.

30. Razzaq, A., Robinson, I.M., McMahon, H.T., Skepper, J.N., Su, Y., Zelhof, A.C., Jackson, A.P., Gay, N.J. and O'Kane, C.J. (2001) Amphiphysin is necessary for organization of the excitation-contraction coupling machinery of muscles, but not for synaptic vesicle endocytosis in Drosophila. *Genes Dev.,* **15,** 2967-2979.

31. Buj-Bello, A., Fougerousse, F., Schwab, Y., Messaddeq, N., Spehner, D., Pierson, C.R., Durand, M., Kretz, C., Danos, O., Douar, A.M. *et al.* (2008) AAV-mediated intramuscular delivery of myotubularin corrects the myotubular myopathy phenotype in targeted murine muscle and suggests a function in plasma membrane homeostasis. *Hum. Mol. Genet.,* **17,** 2132-2143.

32. Dowling, J.J., Vreede, A.P., Low, S.E., Gibbs, E.M., Kuwada, J.Y., Bonnemann, C.G. and Feldman, E.L. (2009) Loss of myotubularin function results in T-tubule disorganization in zebrafish and human myotubular myopathy. *PLoS Genet.,* **5,** e1000372.

33. Al-Qusairi, L., Weiss, N., Toussaint, A., Berbey, C., Messaddeq, N., Kretz, C., Sanoudou, D., Beggs, A.H., Allard, B., Mandel, J.L. *et al.* (2009) T-tubule disorganization and defective excitation-contraction coupling in muscle fibers lacking myotubularin lipid phosphatase. *Proc. Natl. Acad. Sci. U S A,* **106,** 18763-18768.

34. Glover, L. and Brown, R.H. (2007) Dysferlin in membrane trafficking and patch repair. *Traffic,* **8,** 785-794.

35. Capanni, C., Sabatelli, P., Mattioli, E., Ognibene, A., Columbaro, M., Lattanzi, G., Merlini, L., Minetti, C., Maraldi, N.M. and Squarzoni, S. (2003) Dysferlin in a hyperCKaemic patient with caveolin 3 mutation and in C2C12 cells after p38 MAP kinase inhibition. *Exp. Mol. Med.,* **35,** 538-544.

36. Matsuda, C., Hayashi, Y.K., Ogawa, M., Aoki, M., Murayama, K., Nishino, I., Nonaka, I., Arahata, K. and Brown, R.H., Jr. (2001) The sarcolemmal proteins dysferlin and caveolin-3 interact in skeletal muscle. *Hum. Mol. Genet.,* **10,** 1761-1766.

37. Ferguson, S.M., Raimondi, A., Paradise, S., Shen, H., Mesaki, K., Ferguson, A., Destaing, O., Ko, G., Takasaki, J., Cremona, O. *et al.* (2009) Coordinated actions of actin and BAR proteins upstream of dynamin at endocytic clathrin-coated pits. *Dev. Cell,* **17,** 811-822.

38. Mitsunari, T., Nakatsu, F., Shioda, N., Love, P.E., Grinberg, A., Bonifacino, J.S. and Ohno, H. (2005) Clathrin adaptor AP-2 is essential for early embryonal development. *Mol. Cell Biol.,* **25,** 9318-9323.

39. Ohno, H. (2006) Physiological roles of clathrin adaptor AP complexes: lessons from mutant animals. *J. Biochem.,* **139,** 943-948.

40. Ferguson, S.M., Brasnjo, G., Hayashi, M., Wolfel, M., Collesi, C., Giovedi, S., Raimondi, A., Gong, L.W., Ariel, P., Paradise, S. *et al.* (2007) A selective activity-dependent requirement for dynamin 1 in synaptic vesicle endocytosis. *Science,* **316,** 570-574.

41. Turgeon, B. and Meloche, S. (2009) Interpreting neonatal lethal phenotypes in mouse mutants: insights into gene function and human diseases. *Physiol. Rev.,* **89,** 1-26.

42. Dubowitz, V. and Sewry, C. (2007) Muscle biopsy. A practical approach. In Company, W.S. (ed.), *Muscel biopsy A practical approach.* Third ed. Elsevier, London - Philadelphia, pp. 21-39.

43. Trollet, C., Anvar, S.Y., Venema, A., Hargreaves, I.P., Foster, K., Vignaud, A., Ferry, A., Negroni, E., Hourde, C., Baraibar, M.A. *et al.* (2010) Molecular and phenotypic characterization of a mouse model of oculopharyngeal muscular dystrophy reveals severe muscular atrophy restricted to fast glycolytic fibres. *Hum. Mol. Genet.,* **19,** 2191-207.

44. Fraysse, B., Liantonio, A., Cetrone, M., Burdi, R., Pierno, S., Frigeri, A., Pisoni, M., Camerino, C. and De Luca, A. (2004) The alteration of calcium homeostasis in adult dystrophic mdx muscle fibers is worsened by a chronic exercise in vivo. *Neurobiol. Dis.*, **17,** 144-154.

45. Grynkiewicz, G., Poenie, M. and Tsien, R.Y. (1985) A new generation of Ca2+ indicators with greatly improved fluorescence properties. *J. Biol. Chem.,* **260,** 3440-3450.

Legends to figures.

Table 1. Contractile properties of *tibialis anterior* and *soleus* muscles.

P_0: absolute force. sP_0: specific maximum tetanic force. F30%: time for maximal twitch tension to fall by 30%. Statistical comparison was performed using a Mann-Whitney *U*-test. Both TA and *soleus* muscles of each animals were tested (weaning group: n = 4 WT vs 6 HTZ; 2-month-old: n = 6/genotype; 8-month-old n = 3WT vs 6 HTZ). Intra-age statistical analysis: [a]: $P < 0.05$ and [b]: $P < 0.001$ compare to WT. Intra-genotype statistical analysis: [c]: $P < 0.05$, [d]: $P < 0.01$ and [e]: $P < 0.001$ compare to 3 wk; [f]: $P < 0.05$, [g]: $P < 0.01$, and [h]: $P < 0.001$ compare to 2 month-old.

Figure 1. Construction of knock-in *Dnm2*^{R465W} mouse model.

A. Schematic representation of the structure of the wild-type (WT) *DNM2* gene and strategy of homologous recombination (HR) using the targeting vector. The knock-in (KI) allele harbours the p.R465W mutation encoded by exon 11 and a loxP site in intron 11 resulting to the removal of the floxed Neomycin selection cassette (Neo). **B**. Agarose gel electrophoresis of the genotyping PCR using the forward (F) and reverse (R) primers shown in A. The 445 and 533 bp represent the WT and the KI alleles, respectively. **C**. Electrophoregrams of RT-PCR products from hindlimbs total RNA of the 3 genotypes showing expression of the mutation at the transcript level. **D**. Agarose gel electrophoresis of Dnm2 RT-PCR product from total RNA extracted from neonatal hindlimbs and RT-qPCR quantification (n = 5/genotype). P0 was used as control. **E.** Dnm2 western-blot using proteins extracted from neonatal hindlimbs. Vinculin was used as control for densitometry quantification (n = 5/genotype). Both Dnm2 mRNA and protein levels were unchanged in the 3 genotypes. Data are means ± SEM.

Figure 2. Lifespan, locomotor activity and tissue weight.

A. Growth evolution was determined by the follow-up of 33 WT vs 22 HTZ male and 31 WT versus 25 HTZ female mice for 16 months. Male and female HTZ mice showed similar growth when compared to WT mice. **B**. Locomotor activity of male mice using an openfield test (left) and treadmill (right). In the openfield, the mobility period was measured during the 10 min of test. Histogram represents the mobility in percentage of the 10 min (n = 5/genotype at 2 months and n = 4 WT and 7 HTZ at 8 months). In the treadmill test, the duration of stimulated locomotion was timed until arrest (n = 5/genotype at 2 months and n = 3 WT versus 5 HTZ at 8 months). No difference between WT and HTZ mice was found for any tests. **C**. Mean tissue weights in male mice of 3 weeks (n = 4 WT vs 6 HTZ), 2 months (n = 5/genotype), and 8 months of age (n = 4/genotype). Selective and progressive muscle atrophy was observed in HTZ fast muscle whereas *soleus* muscle showed a transient weight increase. *Extensor digitorum longus* was never affected. The tissue weights were normalized by the total body weight (mg/g). *: $P < 0.05$ and ***: $P < 0.001$when compared to WT. Data are means ± SEM.

Figure 3. Transcriptional analysis of atrophy-associated genes and nuclear localization of active FOXO3a in the *tibialis anterior* muscle.

A. Transcript levels at 2 and 8 months of age were determined by RT-qPCR and normalized to P0 expression. Some gene products involved in ubiquitin-proteasome pathway and autophagy were up-regulated at 2 months of age but returned to basal values at 8 months. n = 6-8 /genotype at 2 and 8 months, respectively. * $P < 0.05$ when compared to WT. **B**. Representative images of dephosphorylated-FOXO3a (active form) immunostaining on TA section at 2 months of age. Nuclei were counterstained with DAPI. Arrows indicate FOXO3a-

positive nuclei. **C**. Count of FOXO3a-positive myonuclei normalized to total nuclei labelled with DAPI in 4 WT and 4 HTZ mice at 2 and 8 months of age. The number of counted nuclei in each condition is indicated. The significant increase in number of FOXO3a-positive nuclei at 2 months correlated to the mRNA level increase observed at this age. Data are means ± SEM.

Figure 4. Histomorphology and ultrastructure in adult muscles.

Representative images of muscle sections of TA muscles from WT (A-C) and HTZ (D-I) male mice at 2 (A-F) and 8 (G-I) months of age stained with HE (A, D, G), NADH-TR (B, E, H), and Menad (C, F, I) (n = 4 per genotype and per age). Atrophy of muscle fibers is associated with an accumulation of oxidative activities in the centre of the fibers seen on NADH-TR staining. There is no centrally located nucleus and no increase in endomysial connective tissue. Asterisks indicate the same fiber in 4 serial sections of TA muscles. Scale bars, 50 µm. Electron microscopy was performed on quadriceps muscles from WT (J, L) and HTZ (K, M) at 8 months of age. Transversal sections showed the slight increase in mitochondrial content in the HTZ muscle (K) when compared to the WT (J). Scale bars, 5 µm. Longitudinal sections showed the reduced size of myofibrils in HTZ muscle (M) but with a relatively well conserved structure when compared to WT (L). Scale bars, 1 µm.

Figure 5. Immunocytochemical analysis of WT isolated fibers.

Representative confocal images of immunostaining in the peripheral region of myofibers isolated from FDB and interosseus muscles from 3 WT mice. Dnm2 immunostaining (A, D, G, J, M, P, S) shows a striated expression pattern associated with perinuclear and longitudinally oriented stainings. Subcellular localization of Dnm2 was achieved by co-immunostaining of Dnm2 with various proteins enriched in specialized area of muscle fiber: α-actinin for Z-line labelling (B), DHPRα1 for T-tubules network (E), α-tubulin for

microtubules (H), SERCA1/2 for SR (K), GM130 for cis-golgi (N), α-bungarotoxin for neuromuscular junction (Q), and clathrin CHC17 (T). C, F, I, L, O, R, and U represent the corresponding merged images with DAPI to stain the myonuclei. Scale bars, 10 µm.

Figure 6. Comparative immunostaining in WT and HTZ isolated fibers.

Representative confocal images of immunostaining in myofibers of FDB and interosseus muscles isolated from 3 WT and 3 HTZ mice. Immunostaining were shown for T-tubules markers (DHPR and amphiphysin), sarcoplasmic reticulum markers (RYR1 and SERCA), α-tubulin for microtubule labelling, α-tubulin for MTOC labelling, and the Golgi apparatus marker GM130. Structure of T-tubules system and sarcoplasmic reticulum appears slightly disorganized in heterozygous fibers. Scale bars, 10 µm.

Figure 7. Dynamin2 and dysferlin in isolated fibers.

A. Confocal images in the center of WT and HTZ isolated fibers immunolabelled with Dnm2 and dysferlin (Dysf) antibodies. Overlay images indicate that Dnm2 and dysferlin co-localized in intracellular aggregates in HTZ fibers. 3D-reconstruction in xz and yz axes, centered on the upper aggregate, show that this structure covers a large portion of the fiber. Muscle fibers were isolated from 3 WT and 3 HTZ mice. B. FM4-64 staining in WT and HTZ isolated muscle fibres. Plasma membrane and T-tubule membranes are similarly labelled with the FM4-64 dye in WT and HTZ fibers.

Figure 8. Dysferlin in human muscle biopsies.

Dysferlin immunoreactivity in human muscle biopsies from one healthy control subject, 4 CNM-patients harboring 4 different *DNM2* mutations (p.R465W, p.R369Q, p.R369W, and p.R522H), one neonatal MTM1-CNM patient, one DNM2-Charcot-Marie-Tooth type 2

patient, and one genetically unresolved CNM-patient without *DNM2* mutation. Dysferlin retention was observed in the cytoplasm of all DNM2-related AD-CNM patients. A biopsy from a patient affected by dysferlinopathy in which dysferlin is absent was used as negative control. Scale bars, 50 µm.

Figure 9. Muscular phenotype in homozygous mouse.

Representative images of muscle sections of TA muscles from 1 WT (A-C) and 1 HMZ mice at weaning (D-F) stained with HE (A, D), NADH-TR (B, E), and Menad (C, F). Muscle atrophy, intermyofibrillar disorganization and altered oxidative enzymes activity distribution can be seen. White arrows indicate portion of cytoplasmic devoid of enzymatic activity, red arrows indicate fibers with myofibrillar disturbances and yellow arrow points to a staining centralized to the middle of the fiber (HTZ-like disorganization). Scale bars represents 50 µm. Electron microscopy was performed in quadriceps muscle from WT (G, I) and HMZ (H, J, K, L) at 3 weeks of age. Transversal sections display an accumulation of connective tissue between myofibers in the HMZ muscle (H) when compared to the WT (G). Nuclei are peripherally positioned but the nuclear content appears lighter than that in WT mouse. Scale bars, 10 µm. Longitudinal sections show the smaller size of the myofibrils and mitochondria accumulation in HMZ muscles (J), compared to WT (I). Scale bars, 0.5 µm. Centralized nuclei with accumulation of mitochondria are observed on longitudinal section of the HMZ mouse (K-L). Misalignment and proliferation of reticular structures can also be seen. An increased in tubular structure content is present in the intermyofibrillar space. Scale bars, 2 µm.

Figure 10. Phenotype of mouse embryonic fibroblasts.

A. Gel electrophoresis of RT-PCR products showing that Dnm1, Dnm2 and Dnm3 are all expressed in MEFs from the 3 genotypes (n = 2 / genotype). Brain, in which the three dynamins are expressed, was used as positive control. **B**. Western-blot in MEFs from 2 embryos of each genotype showing the Dnm2 expression whatever the genotype. α-tubulin was used as loading control. **C**. Representative immunostaining of endogenous DNM2 and α-tubulin, and staining of actin network in MEFs of the 3 genotypes. Diffuse Dnm2 labelling in the cytoplasm with some perinuclear accumulation, appears similar in WT, HTZ and HMZ mice. Both microtubule and actin networks are also unaffected. **D**. Fluorescent transferrin (Tfn) uptake after 15 min evidenced a significant alteration of clathrin-dependent endocytosis in HMZ MEFs. Confocal imaging was used to quantify the signal associated with the fluorescent Tfn relative to the total cell area. n = 135 cells. *: $P < 0.001$ compare to WT cells. Data are means ± SEM.

Table 1

Age	Weaning – 3-week-old		2-month-old		8-month-old	
Mice	WT	HTZ	WT	HTZ	WT	HTZ
Tibialis anterior						
Mass (mg)	14.9 ± 0.8	15.4± 0.8	49.9 ± 1.8[d]	39.4 ± 1.4[b,e]	55.7 ± 3.4[d]	41.6 ± 1.1 [b,e]
P_0 indirect (mN)	195.2 ± 13.0	117.4 ± 18.5 [a]	829.0 ± 43.9[e]	487.9 ± 18.6 [b,e]	1153.8 ± 31.3[d,h]	674.2 ± 24.0 [b,e,h]
sP_0 indirect (mN/mg)	12.8 ± 1.6	7.4 ± 0.9 [a]	16.4 ± 0.5	12.1 ± 0.3 [b,e]	21.2 ± 1.6[c,g]	16.3 ± 0.6 [b,e,h]
P_0 direct (mN)	212.2 ± 17.0	111.4 ± 17.5 [a]	843.9 ± 50.5[e]	494.5 ± 16.5 [b,e]	1155.8 ± 27.5 [d,g]	697.5 ± 21.4 [b,e,h]
sP_0 direct (mN/mg)	14.1 ± 2.1	7.0 ± 0.8 [b]	16.7 ± 0.6	12.5 ± 0.3 [b,e]	21.2 ± 1.4 [c,f]	16.8 ± 0.4 [b,e,h]
Soleus						
Mass (mg)	4.2 ± 0.4	3.9 ± 0.3	11.3 ± 0.3[e]	12.1 ± 0.2 [a]	13.0 ± 0.9 [e]	14.0 ± 0.5 [d]
P_0 direct (mN)	80.8 ± 9.0	68.2 ± 8.7	199.3 ± 6.4 [e]	155.7 ± 5.7 [b]	254.7 ± 4.9[d]	245.1 ± 7.4 [e]
sP_0 direct (mN/mm²)	140.1 ± 9.9	127.5 ± 8.4	175.6 ± 7.1 [c]	126.8 ± 6.1 [b]	207.9 ± 11.7 [e,f]	186.7 ± 5.1 [e]
F30% (sec)	60.6 ± 4.3	68.9 ± 7.9	47.1 ± 2.8[c]	42.9 ± 4.3 [d]	47.8 ± 2.1 [c]	49.9 ± 2.9 [c]

Abbreviations List:

CNM: centronuclear myopathy

COX: cytochrome c oxidase

DNM: dynamin

DHPR: dihydropyridine receptor

FDB: *flexor digitorum brevis*

GT: modified gomori trichrome

HMZ: homozygous

HTZ: heterozygous

HE: hematoxylin and eosin

KI: knock-in

MEFs: mouse embryonic fibroblasts

Menad: menadione-linked α-glycerophosphate dehydrogenase

MTOC: microtubule organizing centre

NADH-TR: Reduced Nicotinamide Adenine Dinucleotide-Tetrazolium Reductase

ORO: Oil Red O

PAS: periodic acid schiff

RyR1: ryanodine receptor1

SDH: succinate dehydrogenase

SERCA: sarco endoplasmic reticulum Ca^{2+}-ATPase

SR: sarcoplasmic reticulum

TA: *tibialis anterior*

vs: versus.

Figure 1

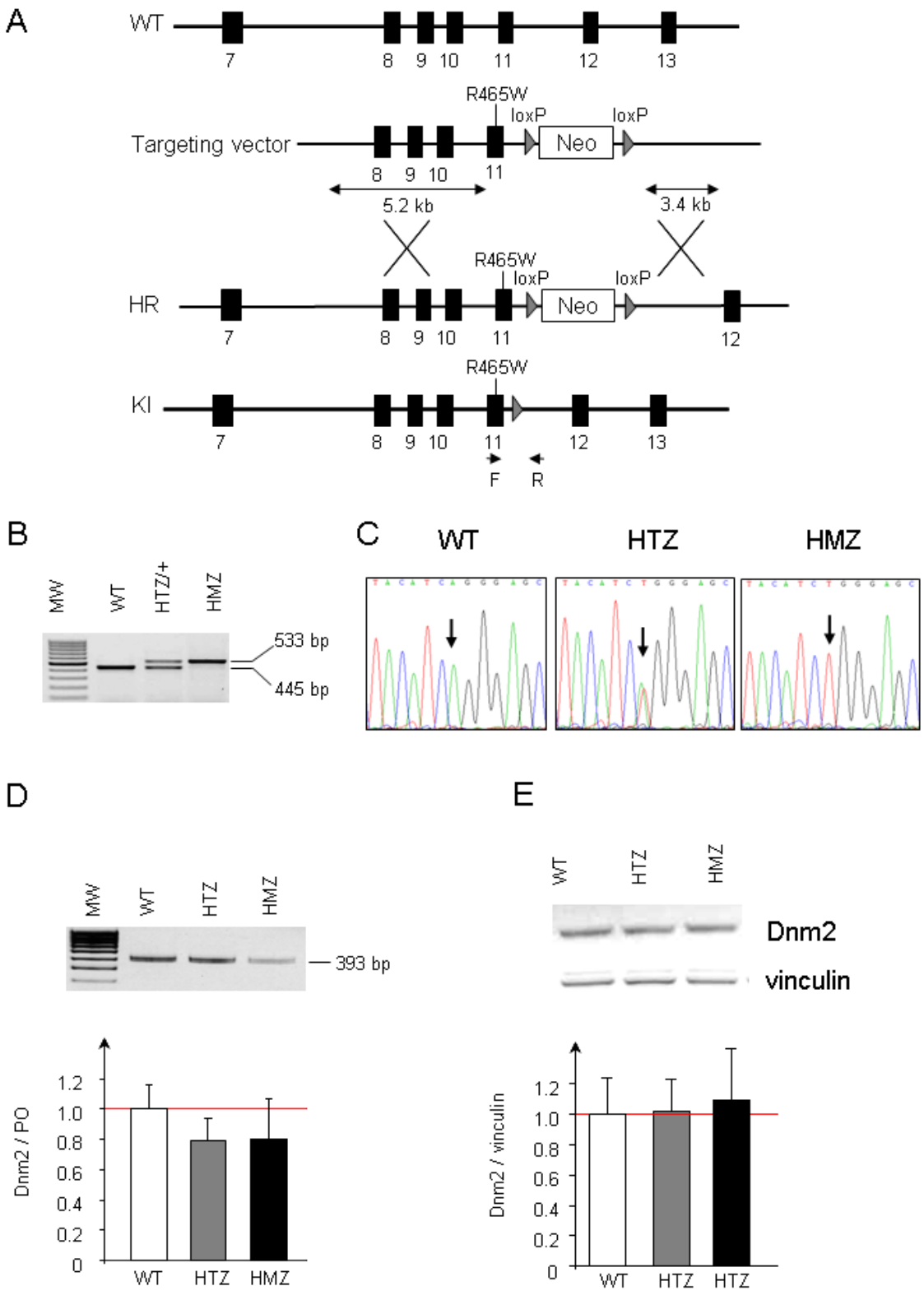
A
WT
7
8
9
10
11
12
13
R465W
loxP
loxP
Targeting vector
Neo
8
9
10
11
5.2 kb
3.4 kb
R465W
loxP
loxP
HR
Neo
7
8
9
10
11
12
R465W
KI
7
8
9
10
11
12
13
F
R
B
MW
WT
HTZ/+
HMZ
533 bp
445 bp
C
WT
HTZ
HMZ
D
MW
WT
HTZ
HMZ
393 bp
Dnm2 / PO
1.2
1.0
0.8
0.6
0.4
0.2
0
WT
HTZ
HMZ
E
WT
HTZ
HMZ
Dnm2
vinculin
Dnm2 / vinculin
1.2
1.0
0.8
0.6
0.4
0.2
0
WT
HTZ
HTZ

Figure 2

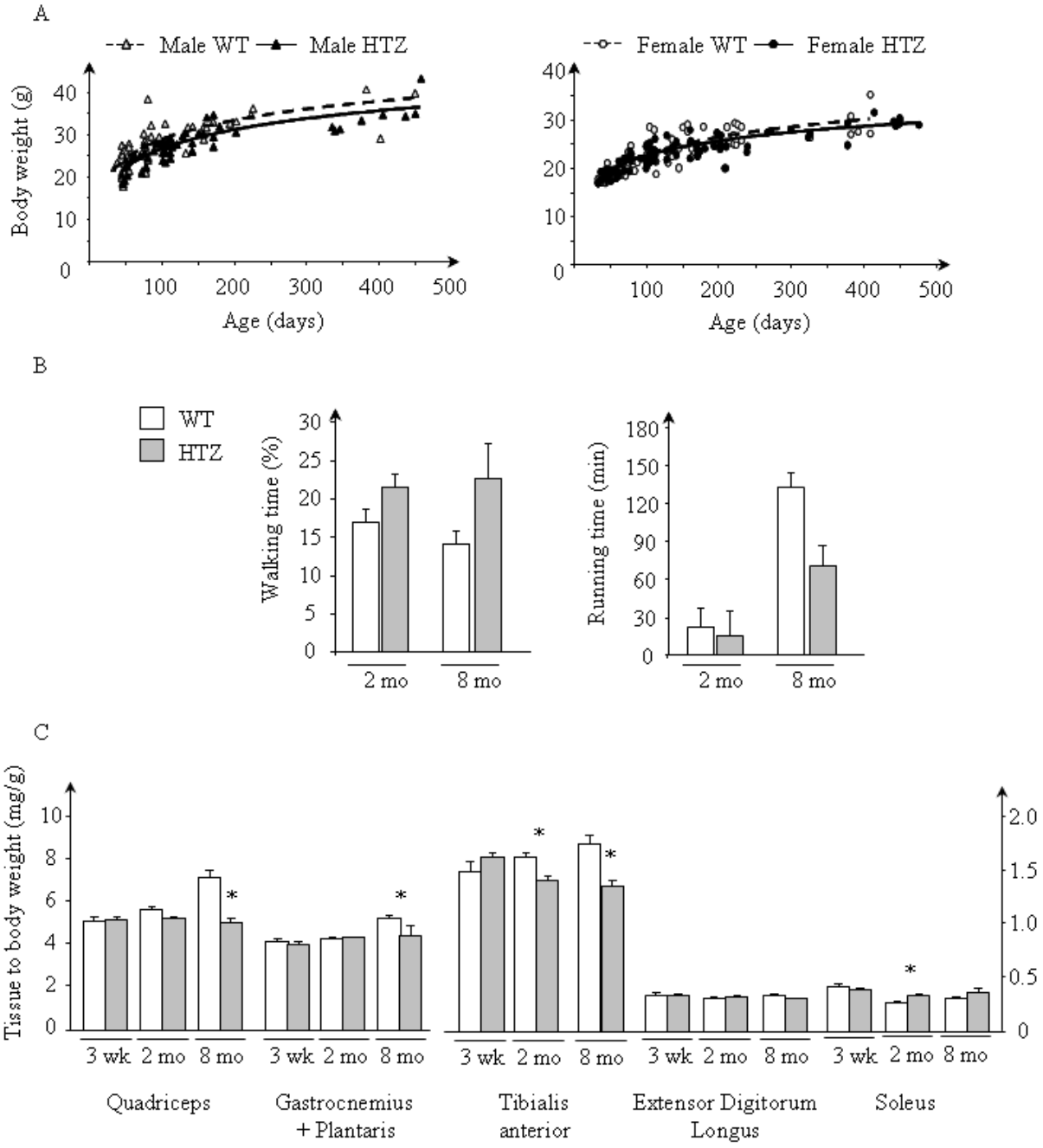
A
Male WT
Male HTZ
Female WT
Female HTZ
Body weight (g)
Age (days)
B
WT
HTZ
Walking time (%)
Running time (min)
2 mo
8 mo
C
Tissue to body weight (mg/g)
3 wk
2 mo
8 mo
Quadriceps
Gastrocnemius + Plantaris
Tibialis anterior
Extensor Digitorum Longus
Soleus

Figure 3

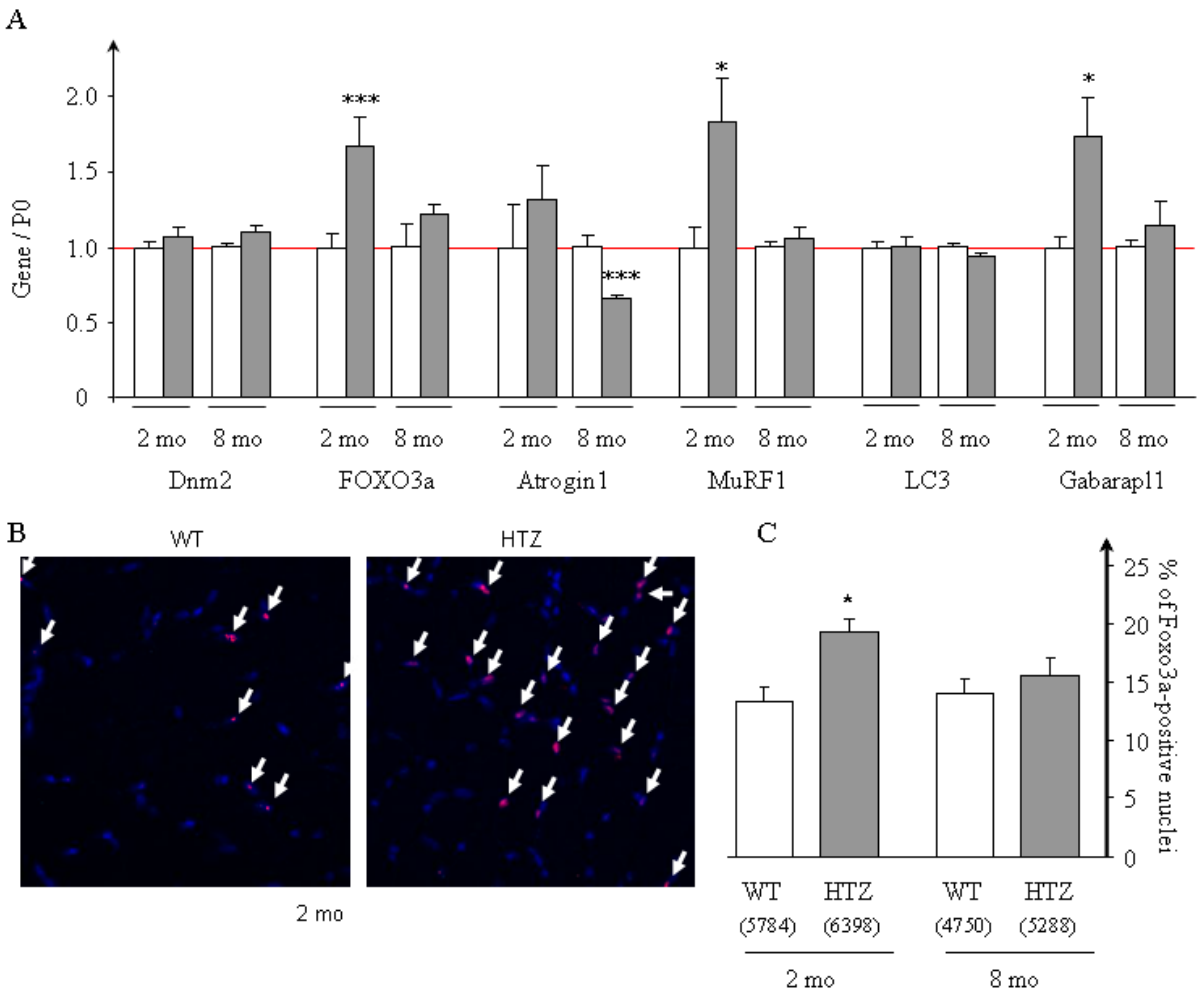
A
Gene / P0
2.0
1.5
1.0
0.5
0
***
***
*
*
2 mo
8 mo
Dnm2
FOXO3a
Atrogin1
MuRF1
LC3
Gabarap11
B
WT
HTZ
2 mo
C
% of Foxo3a-positive nuclei
25
20
15
10
5
0
*
WT
HTZ
WT
HTZ
(5784)
(6398)
(4750)
(5288)
2 mo
8 mo

Figure 4

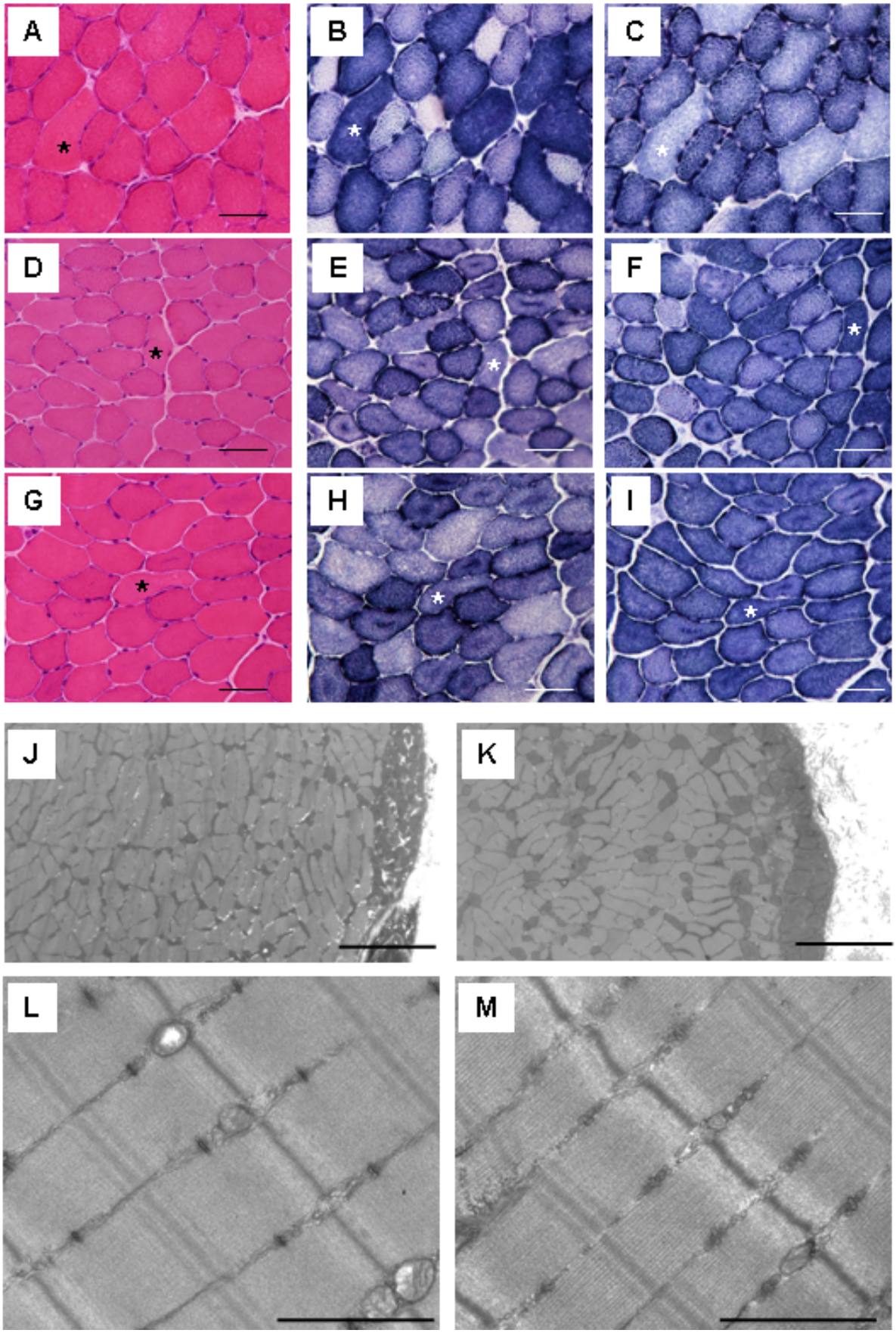

Figure 5

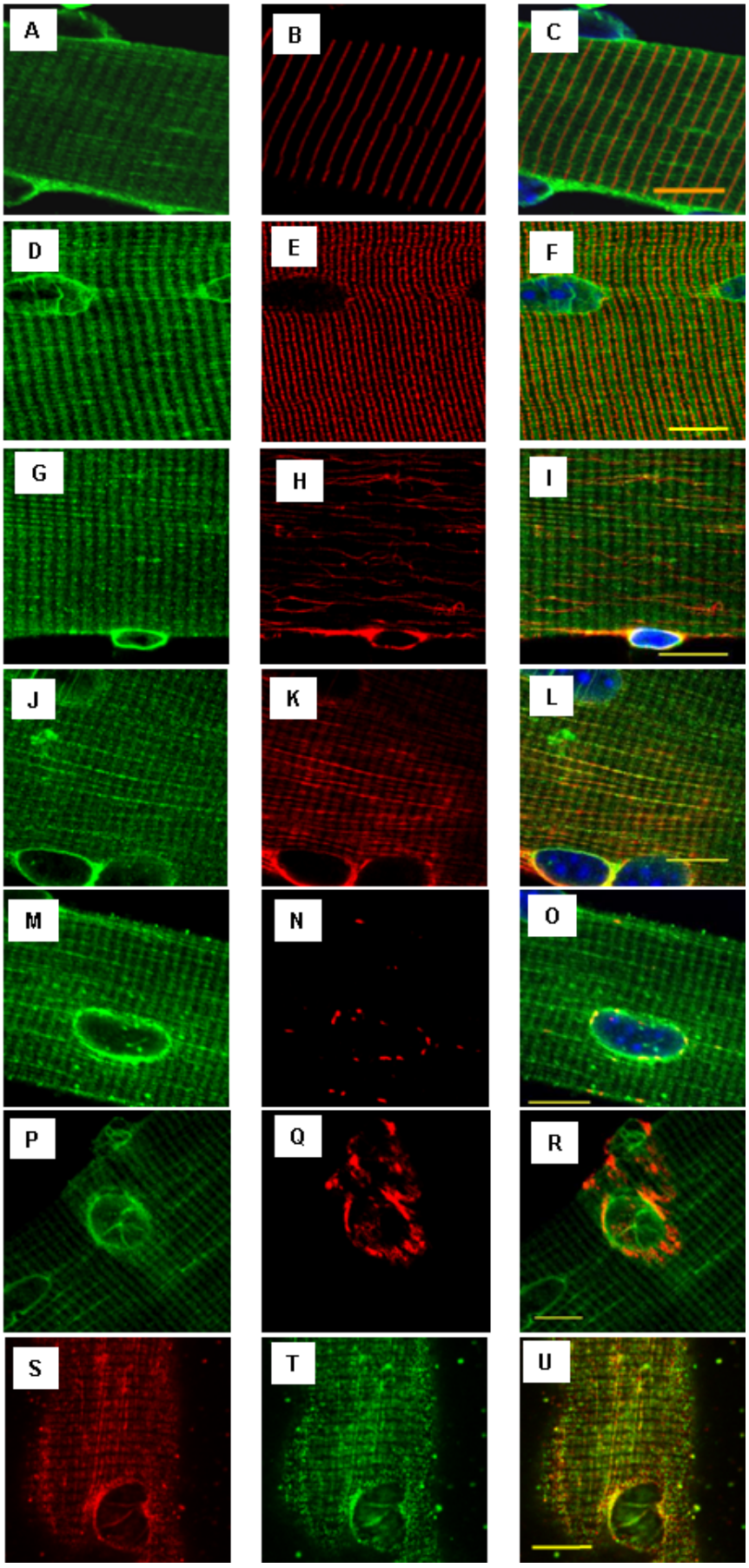

Figure 6

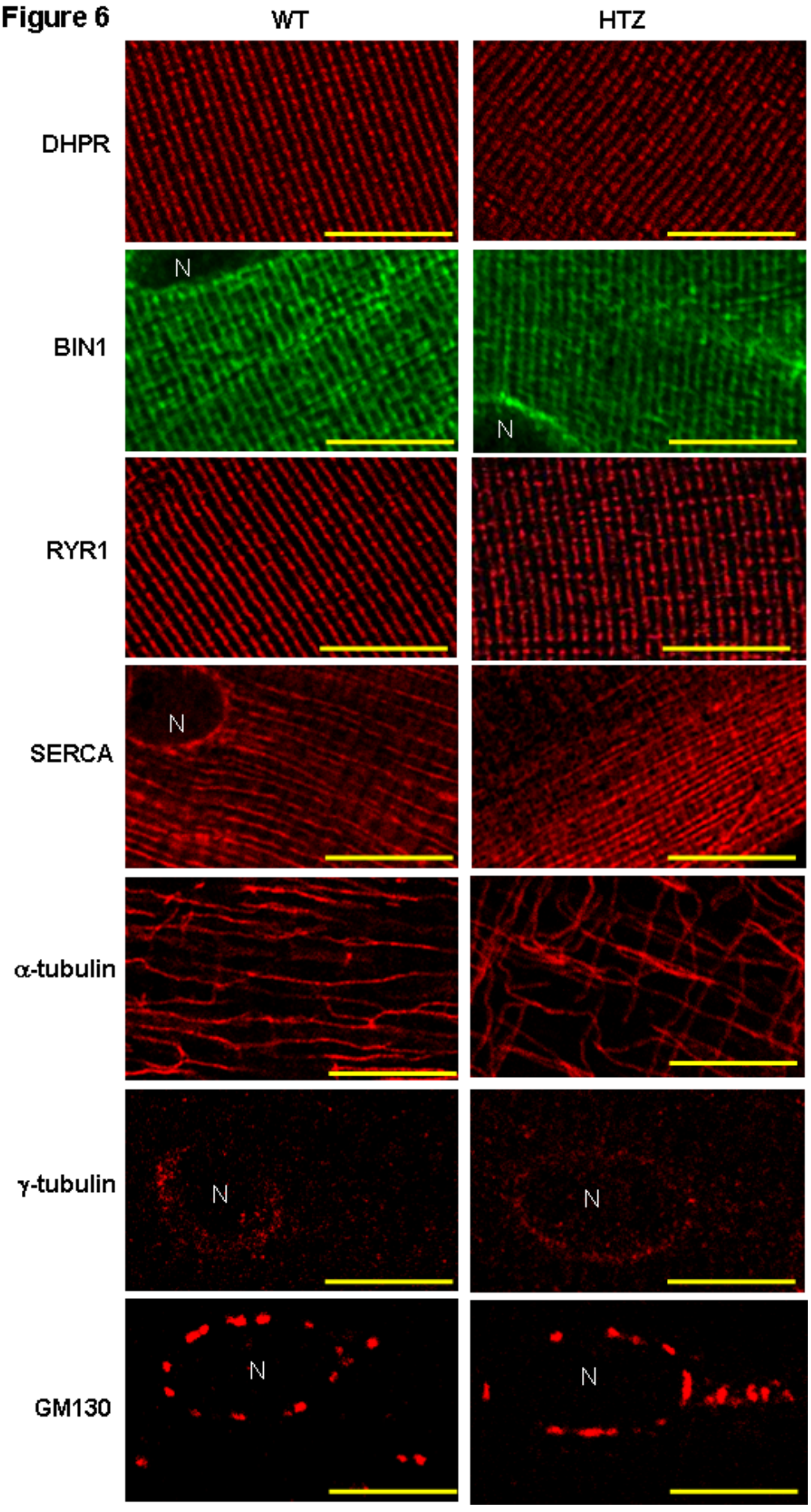

Figure 7

A

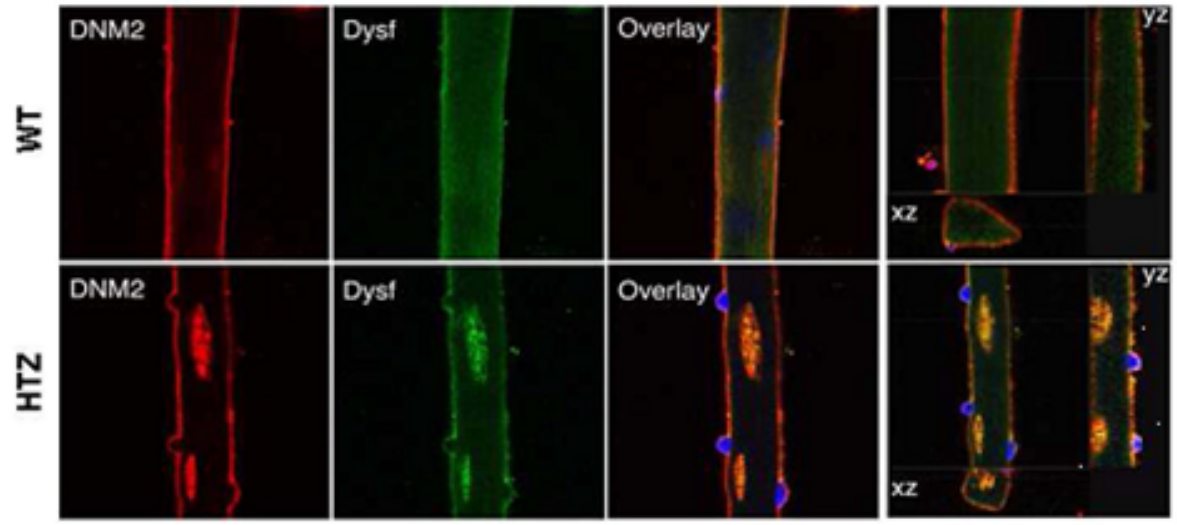

B

Figure 8

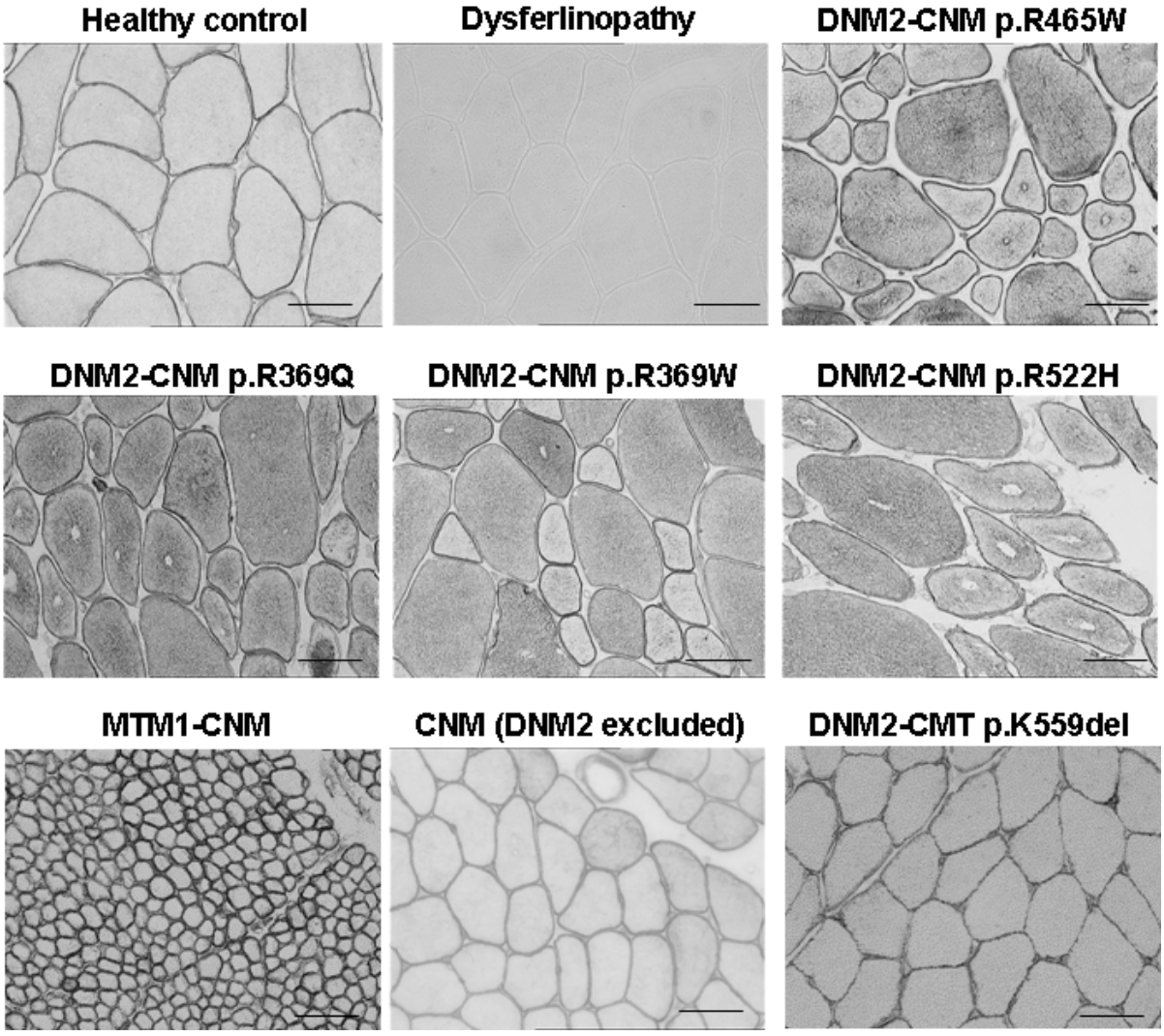
Healthy control
Dysferlinopathy
DNM2-CNM p.R465W
DNM2-CNM p.R369Q
DNM2-CNM p.R369W
DNM2-CNM p.R522H
MTM1-CNM
CNM (DNM2 excluded)
DNM2-CMT p.K559del

Figure 9

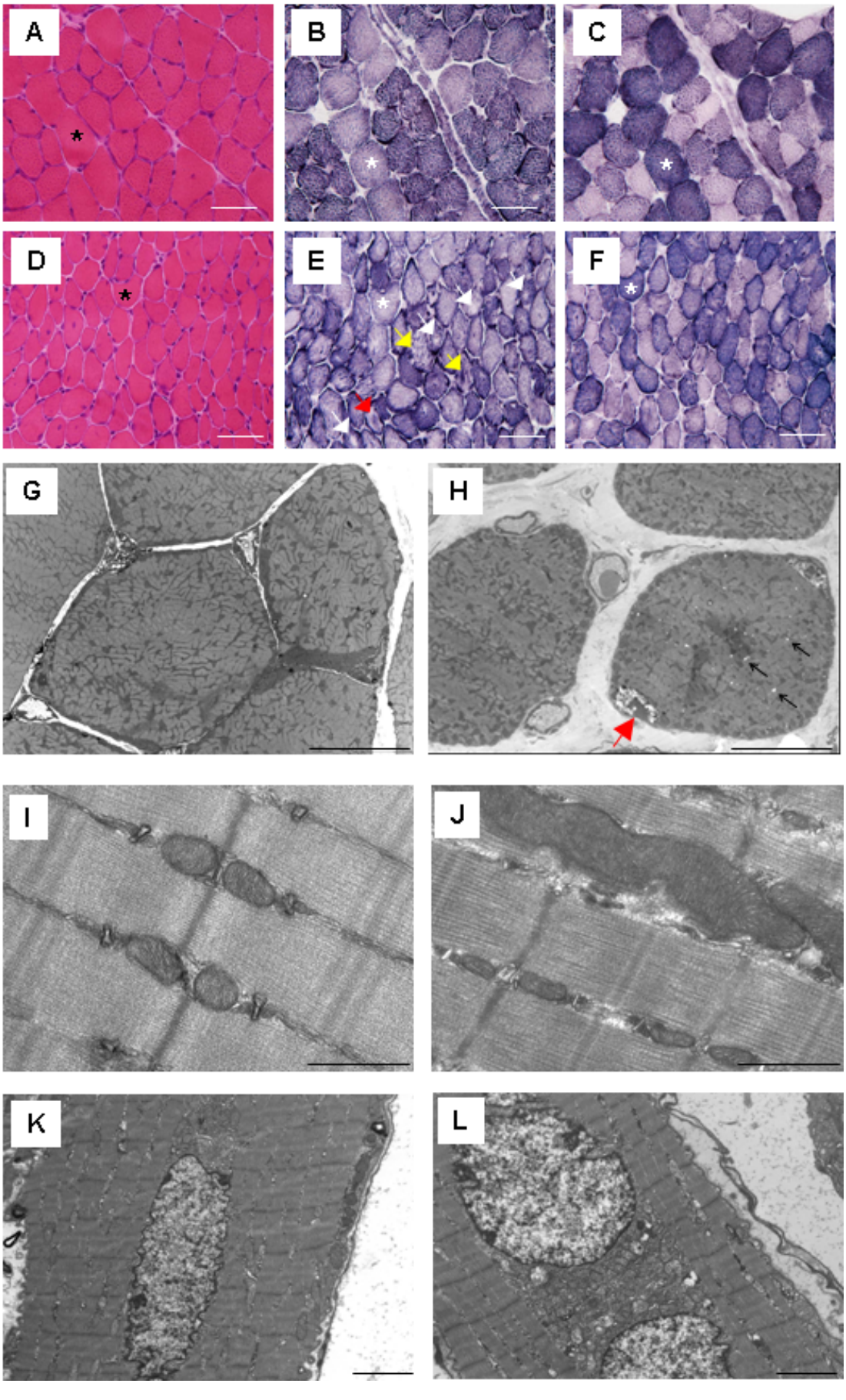

Figure 10

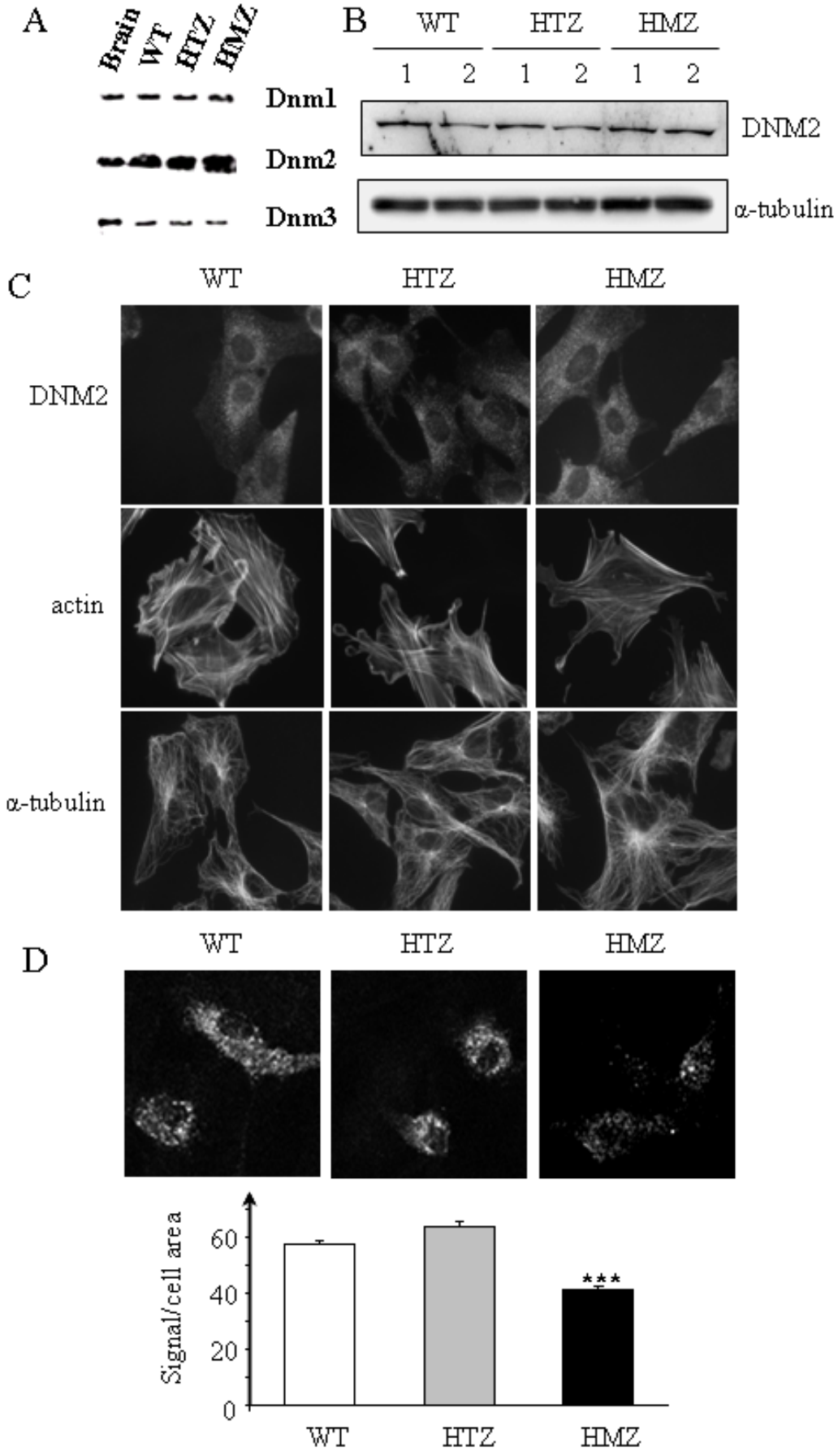
A
Brain
WT
HTZ
HMZ
Dnm1
Dnm2
Dnm3
B
WT
HTZ
HMZ
1
2
1
2
1
2
DNM2
α-tubulin
C
WT
HTZ
HMZ
DNM2
actin
α-tubulin
D
WT
HTZ
HMZ
Signal/cell area
60
40
20
0
***
WT
HTZ
HMZ

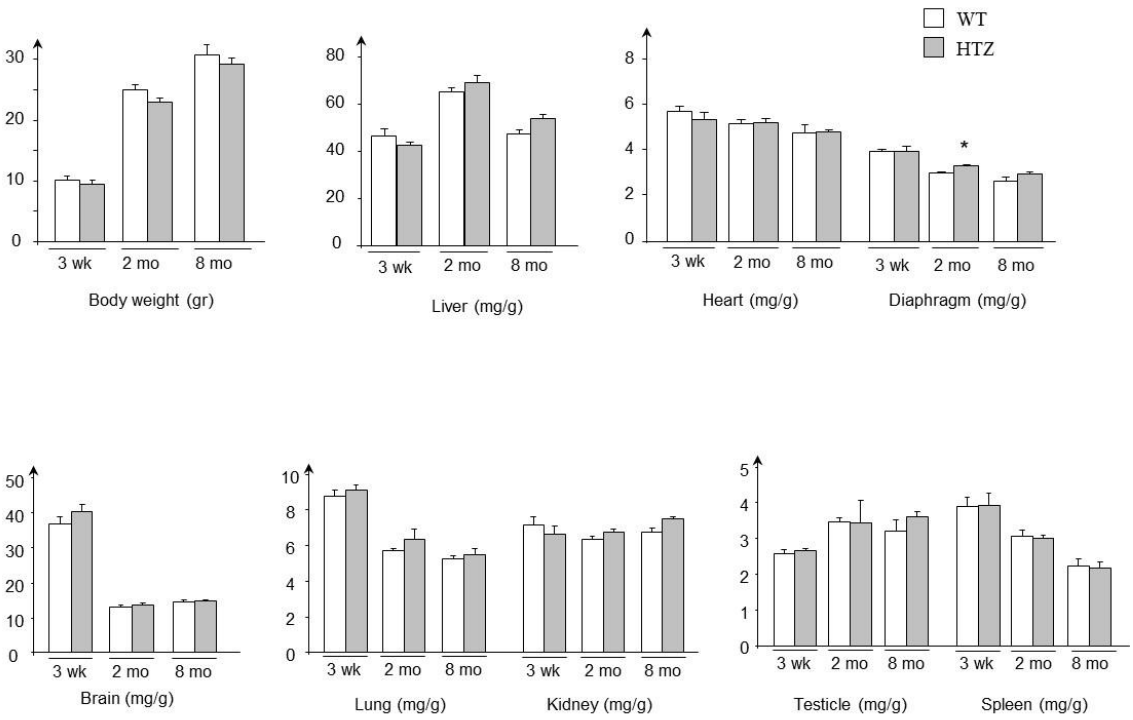
WT
HTZ
Body weight (gr)
Liver (mg/g)
Heart (mg/g)
Diaphragm (mg/g)
Brain (mg/g)
Lung (mg/g)
Kidney (mg/g)
Testicle (mg/g)
Spleen (mg/g)
3 wk
2 mo
8 mo
*

Sup Fig 1

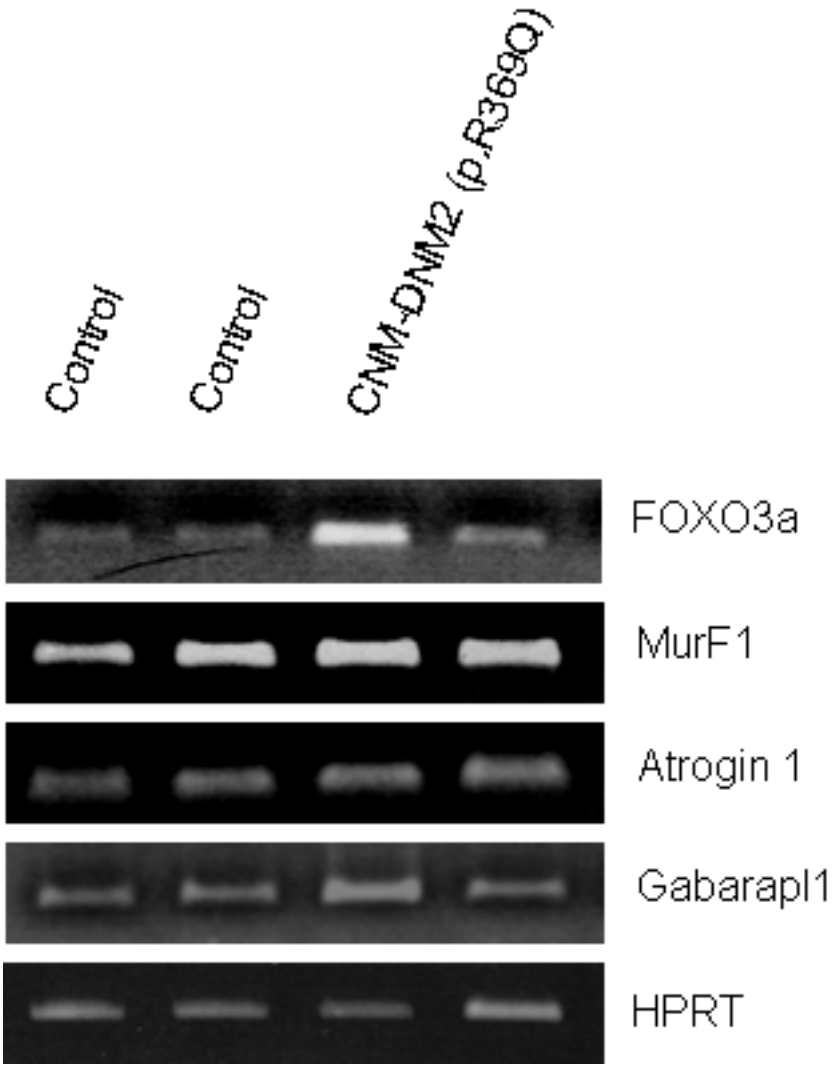
Control
Control
CNM-DNM2 (p.R369Q)
FOXO3a
MurF1
Atrogin 1
Gabarapl1
HPRT

Sup fig 2

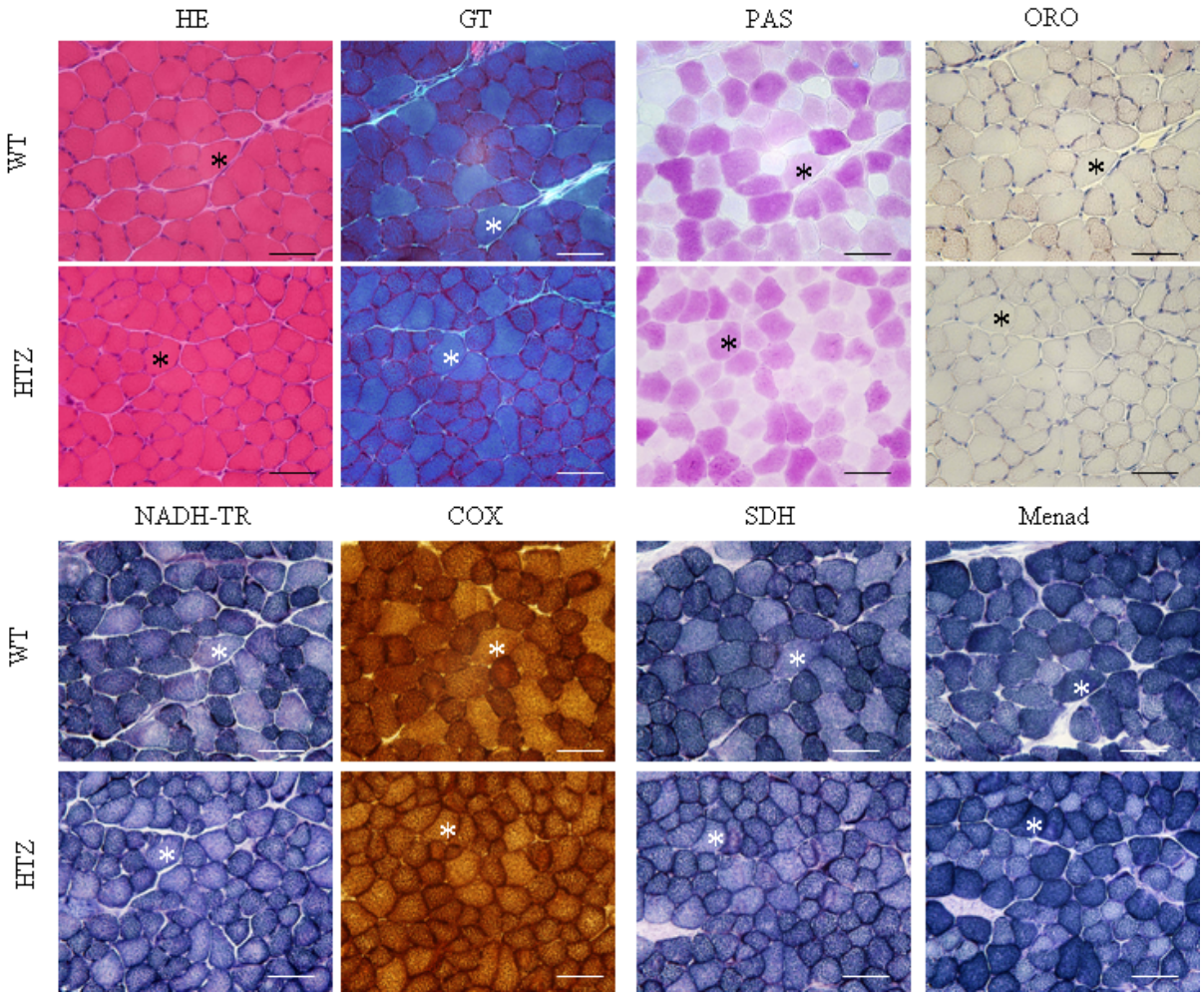

Sup fig 3

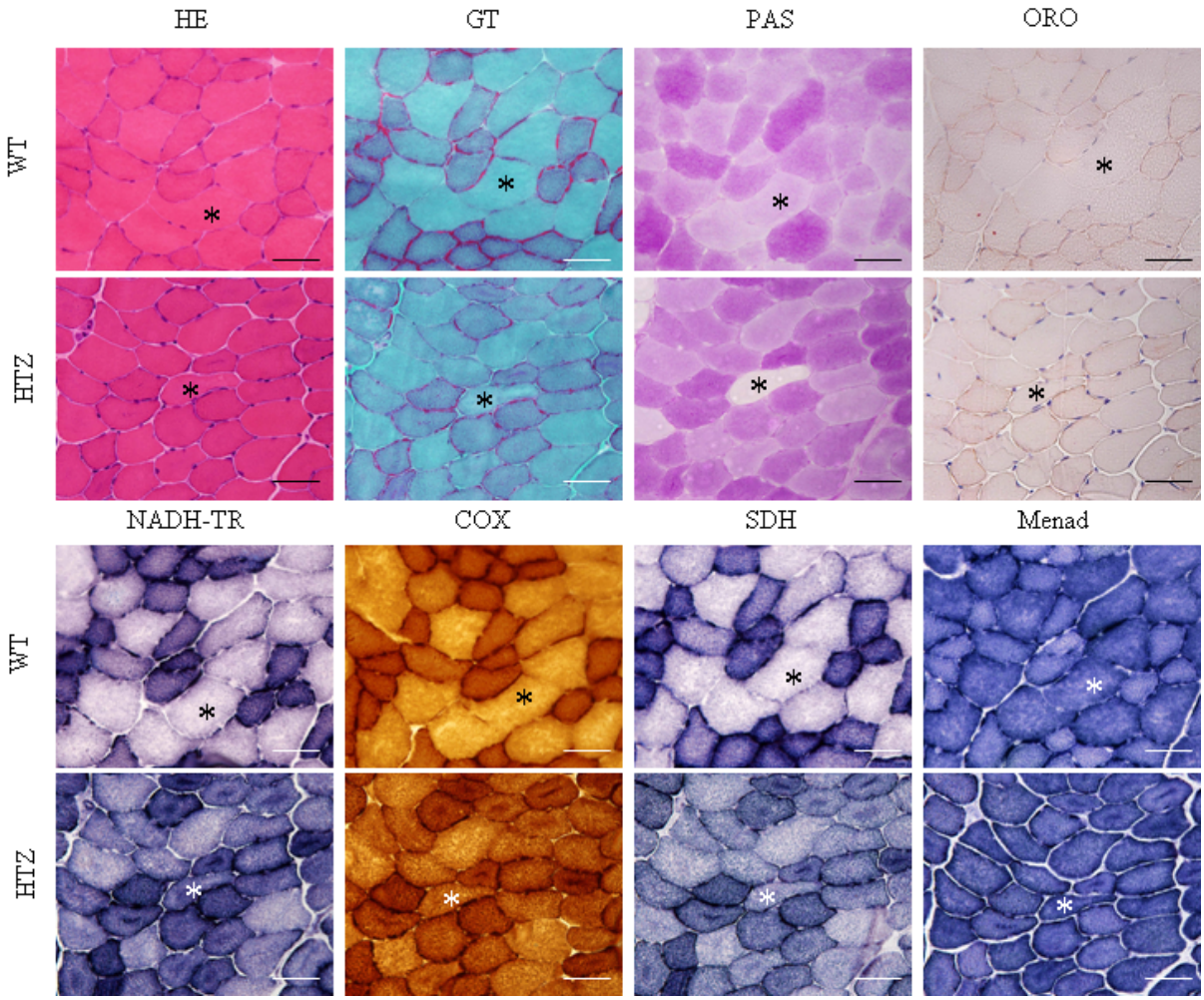

Sup fig 4

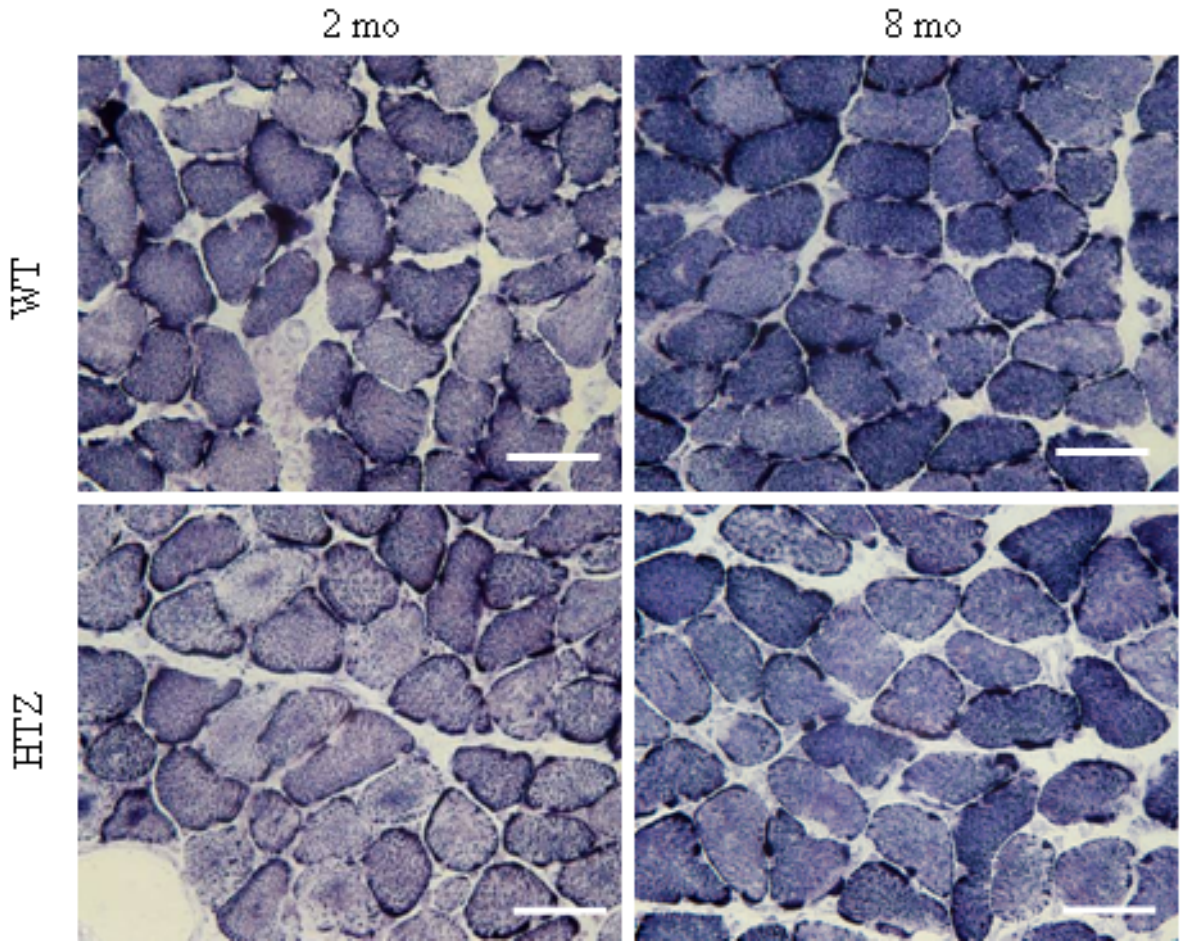

Sup fig 5

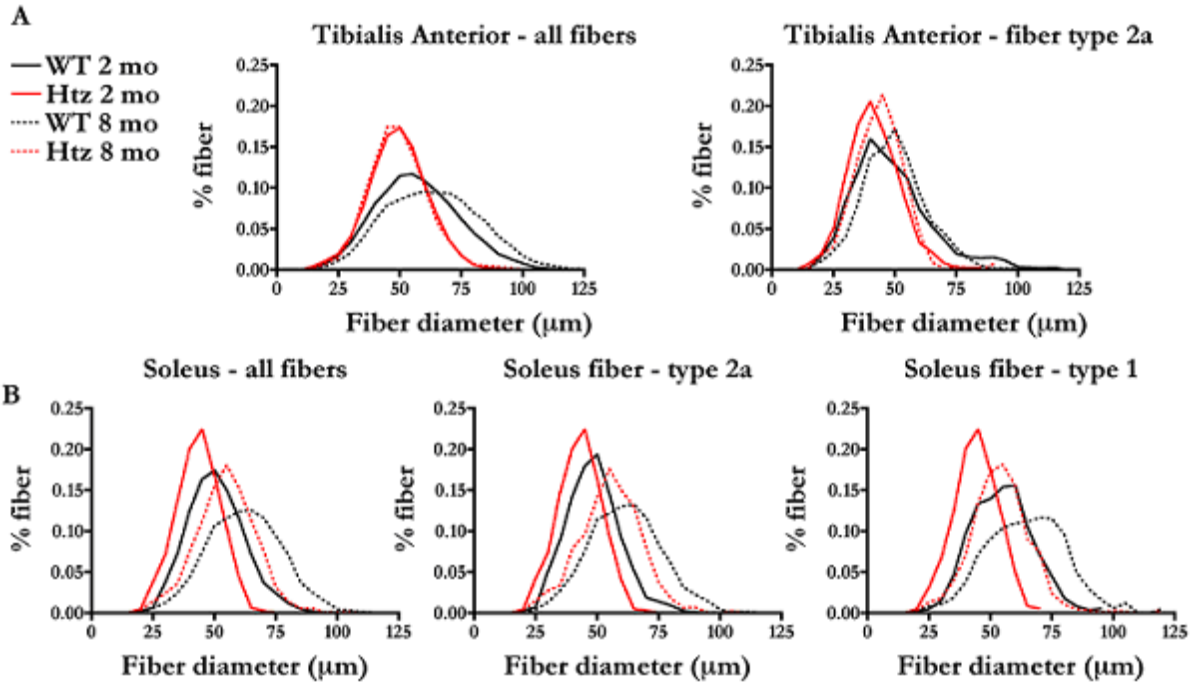
A
WT 2 mo
Htz 2 mo
WT 8 mo
Htz 8 mo
Tibialis Anterior - all fibers
Tibialis Anterior - fiber type 2a
% fiber
Fiber diameter (µm)
B
Soleus - all fibers
Soleus fiber - type 2a
Soleus fiber - type 1

Sup fig 6

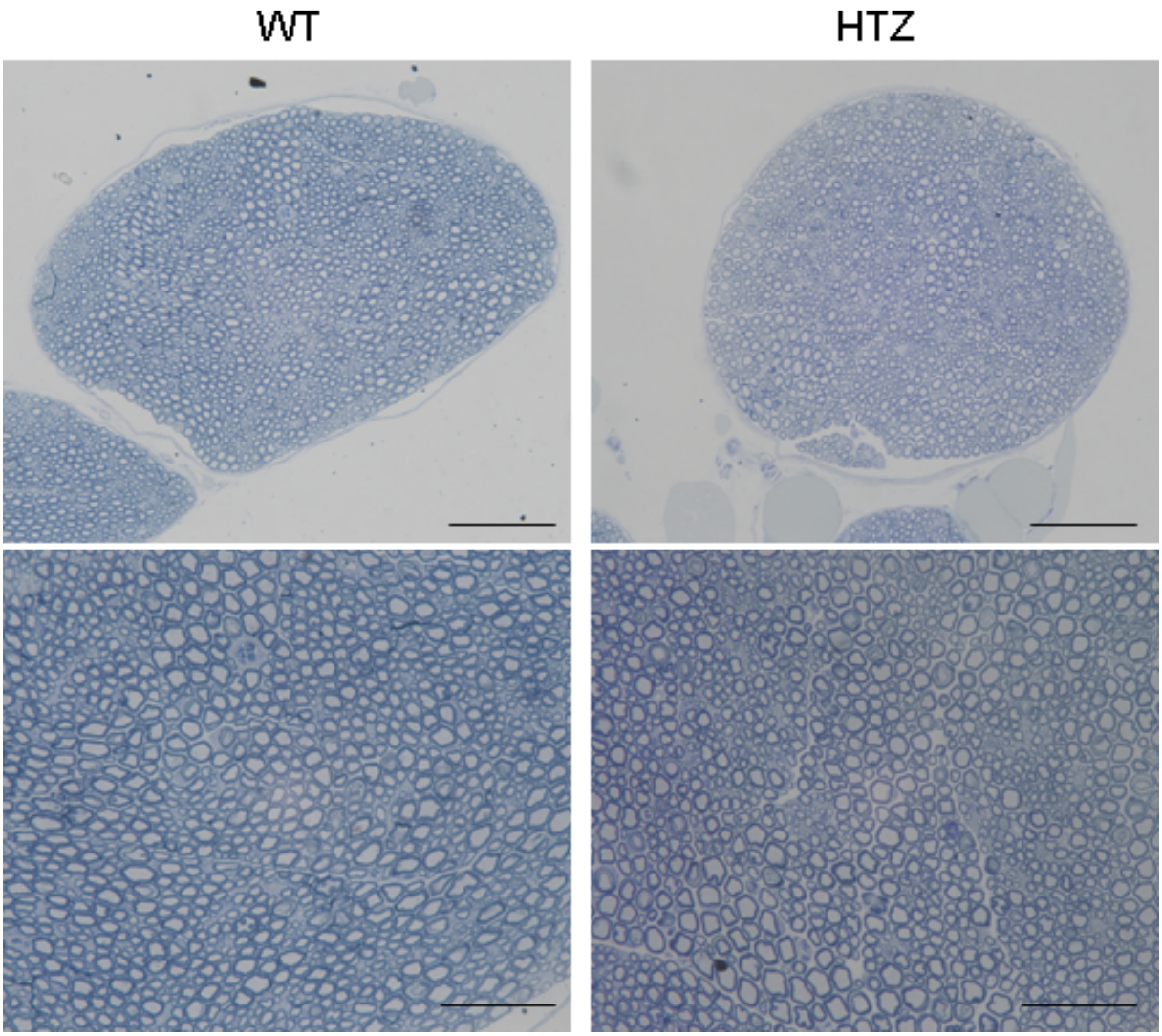

Sup fig 7